

Journal of Geophysical Research: Oceans

RESEARCH ARTICLE

10.1002/2016JC011755

Key Points:

- Shear stresses imposed by roughness on the flow are much larger than those acting on bed sediment
- Suspended sediment concentrations and fluxes are suppressed by the large reef roughness
- Accounting for reduced shear stresses within the roughness improves sediment transport predictions

Correspondence to:

A. W. M. Pomeroy,
andrewpomeroy@gmail.com

Citation:

Pomeroy, A. W. M., R. J. Lowe, M. Ghisalberti, C. Storlazzi, G. Symonds, and D. Roelvink (2017), Sediment transport in the presence of large reef bottom roughness, *J. Geophys. Res. Oceans*, 122, 1347–1368, doi:10.1002/2016JC011755.

Received 26 FEB 2016

Accepted 10 JAN 2017

Accepted article online 20 JAN 2017

Published online 20 FEB 2017

Sediment transport in the presence of large reef bottom roughness

Andrew W. M. Pomeroy^{1,2,3} , Ryan J. Lowe^{1,2,3}, Marco Ghisalberti^{4,5}, Curt Storlazzi⁶ , Graham Symonds^{2,7}, and Dano Roelvink^{8,9} 

¹ARC Centre of Excellence for Coral Reef Studies, University of Western Australia, Perth, Western Australia, Australia,

²School of Earth Sciences, University of Western Australia, Crawley, Western Australia, Australia, ³UWA Oceans Institute, University of Western Australia, Crawley, Western Australia, Australia, ⁴Department of Infrastructure Engineering, University of Melbourne, Melbourne, Victoria, Australia, ⁵School of Civil, Environmental and Mining Engineering, University of Western Australia, Crawley, Western Australia, Australia, ⁶Pacific Coastal and Marine Science Center, U.S.

Geological Survey, Santa Cruz, California, USA, ⁷CSIRO, Oceans and Atmosphere, Wembley, Western Australia, Australia,

⁸Deltares, Delft, Netherlands, ⁹UNESCO-IHE, Delft, Netherlands

Abstract The presence of large bottom roughness, such as that formed by benthic organisms on coral reef flats, has important implications for the size, concentration, and transport of suspended sediment in coastal environments. A 3 week field study was conducted in approximately 1.5 m water depth on the reef flat at Ningaloo Reef, Western Australia, to quantify the cross-reef hydrodynamics and suspended sediment dynamics over the large bottom roughness ($\sim 20\text{--}40$ cm) at the site. A logarithmic mean current profile consistently developed above the height of the roughness; however, the flow was substantially reduced below the height of the roughness (canopy region). Shear velocities inferred from the logarithmic profile and Reynolds stresses measured at the top of the roughness, which are traditionally used in predictive sediment transport formulations, were similar but much larger than that required to suspend the relatively coarse sediment present at the bed. Importantly, these stresses did not represent the stresses imparted on the sediment measured in suspension and are therefore not relevant to the description of suspended sediment transport in systems with large bottom roughness. Estimates of the bed shear stresses that accounted for the reduced near-bed flow in the presence of large roughness vastly improved the relationship between the predicted and observed grain sizes that were in suspension. Thus, the impact of roughness, not only on the overlying flow but also on bed stresses, must be accounted for to accurately estimate suspended sediment transport in regions with large bottom roughness, a common feature of many shallow coastal ecosystems.

1. Introduction

The presence of large bottom roughness over coral reefs directly modifies the near-bed hydrodynamics that are responsible for sediment transport. For typical wave-exposed reefs, cross-reef mean flows (currents) are generated by radiation stress gradients induced by incident short (sea-swell) waves breaking in the surf zone (i.e., waves with periods 5–25 s) and the associated mean water level gradients (wave setup) [e.g., Hench *et al.*, 2008; Lowe *et al.*, 2009b; Symonds *et al.*, 1995]. Smaller incident waves that do not break in the surf zone are transmitted across reef flats as depth-limited waves [e.g., Hardy and Young, 1996], with infragravity waves that emanate from the surf zone also propagating across the reef [e.g., Pomeroy *et al.*, 2012]. The large bottom roughness of reefs can impose substantial drag forces on the mean wave-driven currents, and also attenuate wave heights by frictional dissipation as they propagate shoreward across the reef [e.g., Lowe *et al.*, 2005a; Pomeroy *et al.*, 2012; Rosman and Hench, 2011]. Thus, the hydrodynamic processes that prevail within reef systems are determined by the specific roughness characteristics of a reef, which in turn controls how sediment is transported in these environments.

Suspended sediment at high concentrations can adversely affect a variety of benthic reef organisms via multiple mechanisms. As sediment concentrations in the water column increase, light is attenuated and the spectrum is altered, reducing the efficiency of photosynthetic processes that many reef primary producers rely on for energy production [see Roth, 2014, for a review]. In addition, when the rate of sedimentation is

higher than the rate at which sediment is expelled, coral communities become smothered. This inhibits biotic particle feeding and nutrient uptake rates [e.g., Anthony, 2000] and can eventually lead to mortality [e.g., Weber *et al.*, 2012].

For open (bare) sediment beds lacking large immobile bed roughness, the initiation of sediment transport is directly related to the shear stresses that are exerted on the sediment bed (τ_{bed}). Note that a summary of all notation used in the manuscript is provided in Table 1. Motion is initiated when these bed stresses exceed a critical threshold that is dependent upon sediment properties, namely grain size and sediment density (i.e., as expressed in various forms of the classic Shields equation, *Shields* [1936]). When the vertical velocity component of turbulent eddies is sufficiently large to overcome the particle fall velocity (w_s), sediment is lifted into suspension where it can be more efficiently transported [e.g., *Bagnold*, 1966; *Francis*, 1973; *Van Rijn*, 1984]. Vertical turbulent velocity fluctuations associated with these eddies scale with the

Table 1. Notation

Symbol	Definition
a	Frontal area per unit volume
c	Concentration at elevation z
c_0	Reference concentration at elevation z_{ref} above the bed
d	Vertical height of momentum absorption above the bed
g	Acceleration due to gravity
h	Roughness height
k_N	Nondimensional Nikuradse roughness height
s	Relative density of sediment in seawater
\bar{u}	Mean velocity (current)
\bar{u}, \bar{w}	Oscillatory velocity in maximal and upward directions
u', w'	Turbulent velocity maximal and upward directions
$u_* = \sqrt{\tau/\rho_w}$	Shear velocity
w_s	Particle fall velocity
z	Elevation above the bed
z_0	Bed hydraulic roughness length scale
z_{0a}	Apparent bed roughness length scale due to wave-current interaction
A	Empirical coefficient
B	Empirical coefficient
C_D	Drag coefficient
C_f	Bottom friction coefficient
D	Grain size of interest
D_*	Dimensionless grain size
D_{50}	Median grain size
H	Wave height
P	Rouse parameter
T_p	Peak wave period
z_{ref}	Height for reference concentration c_0
α	Factor that accounts for the probability of sediment suspension
δ	Boundary layer thickness
ε_s	Sediment mixing (diffusion) coefficient
θ	Grain size Shields parameter
κ	Von Karman's constant ≈ 0.40
ν	Kinematic viscosity of water
ν_t	(Turbulent) Eddy viscosity of water
ρ_w, ρ_s	Density of seawater, density of sediment
τ	Horizontal shear stress
τ_{drag}	Shear stress due to bed roughness/features
τ_{grains}	Grain related shear stress
τ_{total}	Total resistance experienced by overlying flow
$\omega = 2\pi/T$	(absolute) radian frequency of the waves
Subscripts	
bed	At the bed
c	Current alone
ig	Infragravity quantity ($25 \text{ s} < T < 250 \text{ s}$)
m	Mean of the enhanced flow due to wave-current interaction
max	Maximum of the oscillatory component of the enhanced flow due to wave-current interaction
rms	Root-mean-squared quantity
$rough$	At the top of the roughness layer (\sim top of the canopy)
sw	Sea-swell quantity ($5 \text{ s} < T < 25 \text{ s}$)
w	Waves alone
∞	Free-stream velocity

horizontal bed stresses, or alternatively the shear velocity ($u_* = \sqrt{\tau_{bed}/\rho_w}$) based on seawater density (ρ_w); therefore, relationships used to predict whether transport occurs usually depend on the magnitude of w_s relative to u_* . Within the water column, in a conventional steady state 1-D (vertical) model, the upward diffusion of sediment is balanced by downward settling. This diffusion is described by the vertical gradient in concentration and a sediment mixing coefficient (ε_s), which can be inferred from various turbulence closure models [e.g., *Van Rijn*, 1993]. Irrespective of the closure model assumed, ε_s is dependent upon the turbulent shear stresses within the bottom boundary layer—the region where sediment particles are predominantly suspended and transported. Hence, τ_{bed} (or u_*) is assumed to control many components of the overall sediment transport process, including (a) whether sediment will initially move, (b) whether that sediment will be suspended, and (c) the vertical distribution of suspended sediment concentration in the water column. Collectively, these components form the basis for modern suspended sediment transport models.

When sediment is interspersed within immobile bed roughness, such as on coral reefs as well as within aquatic vegetation such as a seagrass meadow, the mean and turbulent flow structure is substantially modified adjacent to the bed (i.e., within a “roughness sublayer” or “canopy,” defined as the region where the flow is locally modified by individual roughness elements; *Raupach et al.* [1991]). While the overlying flow may experience increased hydraulic resistance as a result of this roughness, the flow that actually interacts with the underlying bed can be substantially attenuated, which in turn reduces the bed shear stresses [e.g., *Le Bouteiller and Venditti*, 2015]. In aquatic canopies, this flow attenuation can promote sediment deposition, especially when canopy densities are high [e.g., *Gacia et al.*, 1999; *James et al.*, 2004]. A limited number of laboratory studies have quantified how sediment transport is modified by large immobile roughness. Of these studies, most only consider bulk sediment transport quantities (e.g., total transport) and do not explicitly consider how modifications to flow by roughness will alter sediment transport mechanisms that make up these bulk transport rates [e.g., *Baptist*, 2005; *Chen et al.*, 2012; *James et al.*, 2002, 2004; *Kothiyari et al.*, 2009]. In field experiments, the primary focus of most studies has been on how suspended sediment concentrations (SSCs) and/or suspended sediment fluxes (SSFs) measured at specific point locations in the water column are empirically correlated to the local wave and/or current conditions [e.g., *Ogston et al.*, 2004; *Storlazzi et al.*, 2009, 2004; *Suhayda and Roberts*, 1977]. Although such correlations may exist, they do not provide fundamental insight into the quantitative links between the hydrodynamic processes, immobile bottom roughness, and rates of sediment transport. Thus, the dynamics of suspended sediment transport in the presence of large roughness elements, such as coral reefs, remains poorly quantified in natural coastal environments and motivates the present study.

We hypothesize that the drag forces exerted by large immobile roughness overlying a coral reef can significantly reduce shear stresses that are directly exerted on an underlying sediment bed, and as a consequence, traditional measures of bottom stresses on a reef are poor predictors of SSCs and SSFs. The objectives of this study were to: (1) assess the “rough-wall” boundary layer flow dynamics and turbulent shear stresses over a coral reef flat; (2) quantify the grain-size distribution and concentrations of suspended sediment in the water column; and (3) evaluate how modifications to the mean and turbulent flow structure alter suspended sediment grain sizes, SSCs, and SSFs over a rough coral reef flat, including the implications for making robust sediment transport predictions within reef environments.

In section 2, we review rough boundary layer theory and establish how near-bed flow and bed shear stresses are reduced within the roughness elements of a reef, and in turn how this may modify sediment transport. In section 3, we then describe the field experiment conducted on a fringing reef, the instrument configurations, and the data analysis methodologies. The results are described in section 4, and in section 5 we discuss how large immobile roughness affects both SSCs and SSFs. In Section 6, we conclude with a discussion of implications of this study for making robust prediction of suspended sediment transport on coral reefs and other analogous benthic ecosystems with large bottom roughness.

2. Background: Flow Structure and Sediment Transport Within Rough-Wall Boundary Layers

2.1. Unidirectional Flow

A rough-wall turbulent boundary layer associated with a unidirectional current can be partitioned into an inertial sublayer and roughness sublayer (Figure 1a). The inertial sublayer, often called the logarithmic layer,

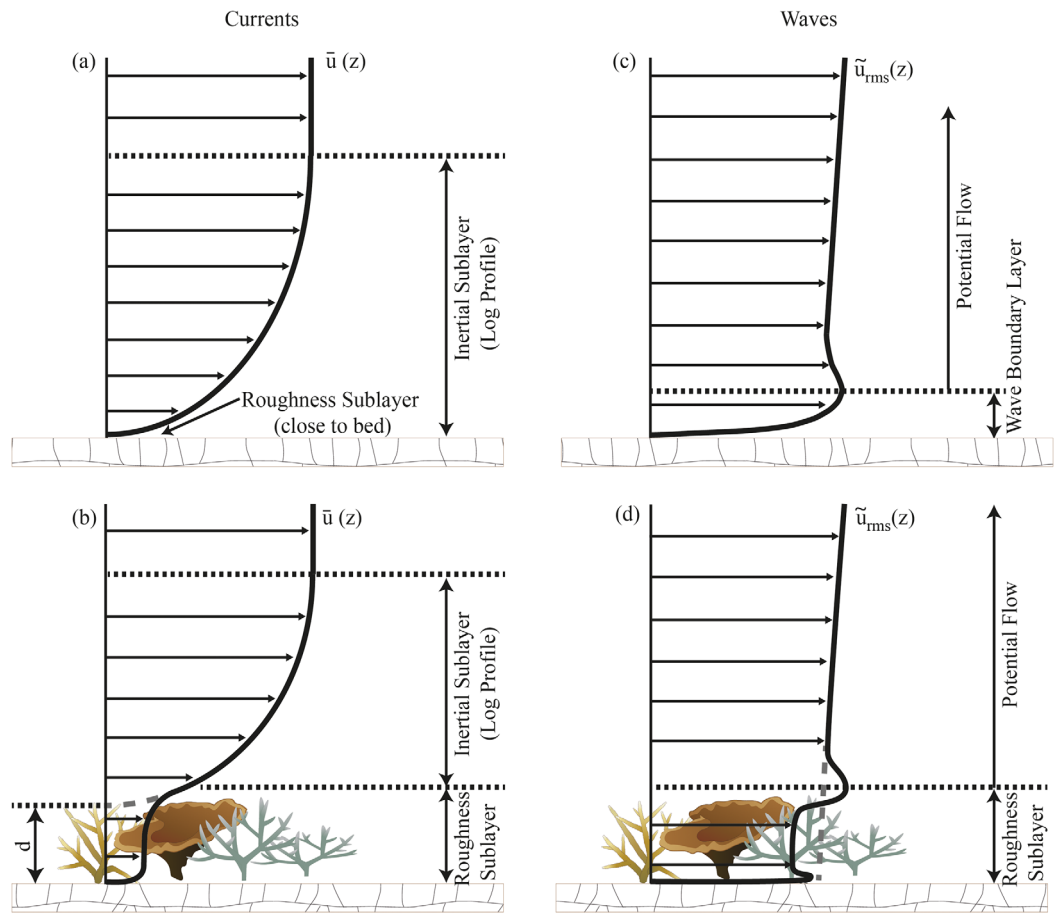


Figure 1. Conceptual model of the boundary layer flow structure for (top) bare beds and (bottom) beds with large roughness under (left) unidirectional (current) and (right) wave-dominated (oscillatory) flow conditions.

develops above the roughness sublayer where the individual roughness elements no longer directly affect the flow and the mean velocity (\bar{u}) profile tends to be governed by the “law of the wall” [e.g., Raupach *et al.*, 1991]:

$$\bar{u} = \frac{u_{*c}}{\kappa} \log \left(\frac{z-d}{z_0} \right) \quad (1)$$

where z is height above the bed; κ is Von Karman’s constant; d is the vertical displacement of the mean velocity profile that relates to the penetration of momentum into the roughness; and z_0 is a hydraulic roughness parameter. In equation (1), the shear velocity u_{*c} is a measure of the turbulent shear stress at the top of the roughness and thus is equivalent to the resistance imposed by the roughness on the overlying current (note the subscript c will denote variables associated with currents).

The roughness sublayer is strongly influenced by the drag imposed by the roughness elements, which if modeled as simple geometric elements (e.g., cubes, cylinders) can be described as a function of the roughness height h , frontal area per unit volume a and a drag coefficient C_D [e.g., Nepf *et al.*, 2007]. When the bottom roughness is relatively small (i.e., C_{Dah} is less than $O(10^{-2})$), such as over a flat sandy bed, the mean height of momentum absorption is located near the base of the roughness ($d \approx 0$) and $u_{*c} \approx u_{*c,bed}$, where $u_{*c,bed}$ is the bed shear velocity (Figure 1a). However, when the roughness is relatively large (i.e., C_{Dah} exceeds $O(10^{-2})$), the drag forces exerted by the roughness elements attenuate the spatially averaged flow (see reviews by Finnigan [2000] and Nepf [2012]). This attenuation results in an inflection of the mean velocity profile at the top of the roughness where the maximum turbulent Reynolds shear stresses are also located. In this case, u_{*c} in equation (1) no longer describes the shear stress acting on the bed, but rather the local turbulent shear stress at the top of the roughness (i.e., $u_{*c} \approx u_{*c,rough}$, Figure 1b). Thus, within the

roughness sublayer (or canopy), the reduction in flow can substantially reduce the shear stresses that are exerted on an underlying sediment bed ($\tau_{c,bed}$).

2.2. Wave-Dominated Flow

When surface waves propagate over a rough seafloor, a wave boundary layer (WBL) of thickness δ_w develops close to the bed (note the subscript w will denote variables associated with waves). Due to the oscillatory nature of the flow, wave-generated turbulence within the WBL can only experience limited vertical growth. A variety of forms for the eddy viscosity within the WBL have been proposed, but one of the simplest and most widely used is that of *Grant and Madsen* [1979], where a representative (time-invariant) value is assumed. Based on this description, when the roughness is relatively small, δ_w is governed by the maximum shear velocity imposed by the wave flow (u_{*w}) and the wave angular frequency (ω); i.e., $\delta_w \sim \kappa u_{*w} / \omega$. The thin nature of the WBL generates larger bed shear stresses ($\tau_{w,bed}$) when compared to a unidirectional current of equivalent magnitude (Figure 1c).

Most research with waves has investigated how large roughness modifies the phase-dependent wave flow structure within the canopy region. Laboratory experiments with idealized canopies [e.g., *Lowe et al.*, 2005b, 2008; *Luhar et al.*, 2010] and field experiments in seagrass canopies [e.g., *Infantes et al.*, 2012] have demonstrated that the attenuation of the root-mean-squared (RMS) wave orbital velocities within the canopy is always less than that of a unidirectional flow of equivalent magnitude. This is due to the wave-driven oscillatory pressure gradient, which is opposed by both canopy drag and inertial forces [e.g., *Lowe et al.*, 2005b; *Zeller et al.*, 2015]. Furthermore, wave phase-dependent Reynolds stresses are enhanced near the top of the roughness and then decrease toward zero within the canopy before they increase again near the bed [e.g., *Lowe et al.*, 2008; *Luhar et al.*, 2010]. This stress profile suggests that for large roughness, two WBLs develop: a larger WBL near the top of the canopy (or roughness layer) and another, thinner, WBL near the bed (Figure 1d).

2.3. Wave-Current Boundary Layers

The superposition of both waves and mean currents nonlinearly combine to modify the turbulent flow structure near the bed and enhance bed shear stresses. Over a wave cycle, the mean of these enhanced stresses (τ_m) is larger than pure current stresses (τ_c), and the maximum of the enhanced stresses (τ_{max}) is larger than the vector summation of τ_c and τ_w [e.g., *Soulsby and Clarke*, 2005].

A variety of wave-current interaction models have been proposed. Most of these models describe the turbulent flow structure over a bed with relatively small bed roughness, i.e., where the roughness height is small relative to the wave-current boundary layer thickness. These models are generally based on semi-empirical eddy viscosity profiles [see *Wiberg*, 1995, for a review]. Under combined wave-current flow, a thin WBL of thickness δ_{max} exists that is controlled by u_{*max} . Above this WBL ($z > \delta_{max}$), the mean velocity profile maintains a logarithmic form described by equation (1); however, with u_{*c} instead replaced with the wave-enhanced mean velocity (u_{*m}) and z_0 replaced with an apparent roughness length (z_{0a}) that is also enhanced by the wave-induced turbulence near the bed relative to a pure unidirectional current [e.g., *Grant and Madsen*, 1979].

The dynamics of wave-current interactions that occur within large roughness (canopies) are still not well-established. However, it is reasonable to assume that the drag imposed by large roughness elements will cause greater attenuation of the current-component of the flow relative to the wave-component, which is supported by experimental observations [e.g., *Lowe et al.*, 2005b, 2008; *Zeller et al.*, 2015]. Thus, under wave-current conditions the flow within the roughness should be more strongly influenced by the contribution of the waves than the current. Similar arguments can be made to describe the flow structure near the top of the roughness and further up in the water column. At a sufficient height above a canopy, the flow structure should be analogous to a classic rough-wall wave-current boundary layer, with a logarithmic mean current profile defined by u_{*m} and z_{0a} that are enhanced by wave-induced turbulence generated within the canopy.

2.4. Sediment Transport in the Presence of Large Roughness

The total resistance experienced by the overlying flow (τ_{total}) is often partitioned into two components: (1) a bed stress component (τ_{bed}) that is due to the stress imposed by sediment grains at the bed; and (2) a form drag component (τ_{drag}) that is due to drag forces either by mobile bed forms [e.g.,

Van Rijn, 2007] or by immobile roughness (e.g., coral structures or aquatic vegetation, Le Bouteiller and Venditti, 2015].

$$\tau_{total} = \tau_{bed} + \tau_{drag} \quad (2)$$

In the presence of relatively small roughness (e.g., the sand grains themselves), τ_{drag} is small and $\tau_{total} \approx \tau_{bed}$; thus the shear stress exerted on overlying flow is equally relevant to the assessment of sediment transport. However, when the roughness is large, τ_{drag} can be substantially greater than τ_{bed} ; in this case the shear stress estimated from hydrodynamic measurements obtained higher in the water column, which includes the large form drag exerted by the roughness (i.e., τ_{total}), is not necessarily related to the stress exerted on the sediment. This has been demonstrated in idealized laboratory experiments where stresses inferred from law-of-the-wall fitting of the velocity profile above roughness have been shown to significantly overestimate bed load sediment transport [e.g., Le Bouteiller and Venditti, 2015], as well as the capacity of a unidirectional flow to suspend and transport sediment when compared to the same flow over a bare sediment bed [e.g., Bouma *et al.*, 2007]. Thus, while the mobilization and suspension of sediment from the bed is broadly governed by the same physical processes (irrespective of whether the roughness is either large or small), these key differences between bed shear stresses should have important implications for rates of sediment transport, and notably the applicability of existing predictive formulae to environments with large roughness.

3. Methods

3.1. Site Description

A 3 week field experiment (27 July to 14 August 2013) was conducted in the northern region of Ningaloo Reef in Western Australia, focusing on a ~5 km section of reef near Tantabiddi (21°52'6"S, 113°58'58"E, Figure 2a). The study specifically focused on a section of reef bounded to the north and south by shore-normal channels (~6 m deep) that cut into the reef crest and outer reef flat. At this site, the cross-shore orientation of the reef is ~130° (defined as clockwise from true north), with the reef crest located 2.0–2.5 km from the shoreline. The reef flat is ~0.6–1.5 m below mean sea level and is ~500 m wide. The lagoon varies in width along the coast due to the presence of a shoreline salient, and is generally ~3 m deep. In contrast to many parts of southern Ningaloo Reef that typically have near 100% coral coverage, this site was specifically chosen as, like many reef systems worldwide, it contained a mix of macro-algae, coralline algae, sand, and some live coral [Cuttler *et al.*, 2015].

3.2. Field Study

The field study consisted of two main components: (1) a detailed study of the hydrodynamics and sediment transport of the reef flat, and (2) a broader-scale hydrodynamic and sediment transport study throughout the reef and lagoon [Pomeroy, 2016]. The results presented in this paper focus on the first component, which was based on intensive sampling conducted on the reef flat (S2, Figure 2b) that was designed to quantify the fine-scale sediment dynamics over the reef.

A “sawhorse” instrument frame was deployed at S2 in a water depth of ~1.5 m (Figures 2e and 2f). Here the bed roughness is ~20–40 cm high. Hydrodynamic measurements were obtained using three vertically distributed Nortek acoustic Doppler velocimeters (ADVs). The bottom ADV was located within the roughness sublayer ($z = 0.2$ m), the middle ADV was located near the top of the roughness elements ($z = 0.5$ m) and the top ADV was located high in the water column ($z = 0.8$ m). The ADVs sampled at 8 Hz for 2048 s each hour. In addition to the ADVs, an upward facing Nortek high-resolution acoustic Doppler profiler (ADP) located slightly to north (~2 m) of the sawhorse frame sampled continuously at 1 Hz using 25 mm bins with the bottom bin located 0.22 m above the bed. Suspended sediment concentrations were inferred from three WetLabs ECO-FLNTU optical backscatter sensors (OBSs) that sampled at 0.3 Hz for 20 min each hour. Suspended sediment samples were collected *in situ* using a suction sampling array that consisted of six 5 mm diameter intakes that were vertically positioned with logarithmic spacing, oriented perpendicular to the dominant mean flow direction, with water pumped to a scaffold platform nearby. Based on the intake diameter and volume flow rate, the intake flow velocity was approximately 0.6 m s^{-1} , or 2–3 times greater than measured root-mean-squared (RMS) velocities (see below); therefore, errors due to inefficiencies or bias in particle capture are expected to be small [Bosman *et al.*, 1987]. A summary of the instrumentation and sampling information is provided in Table 2.

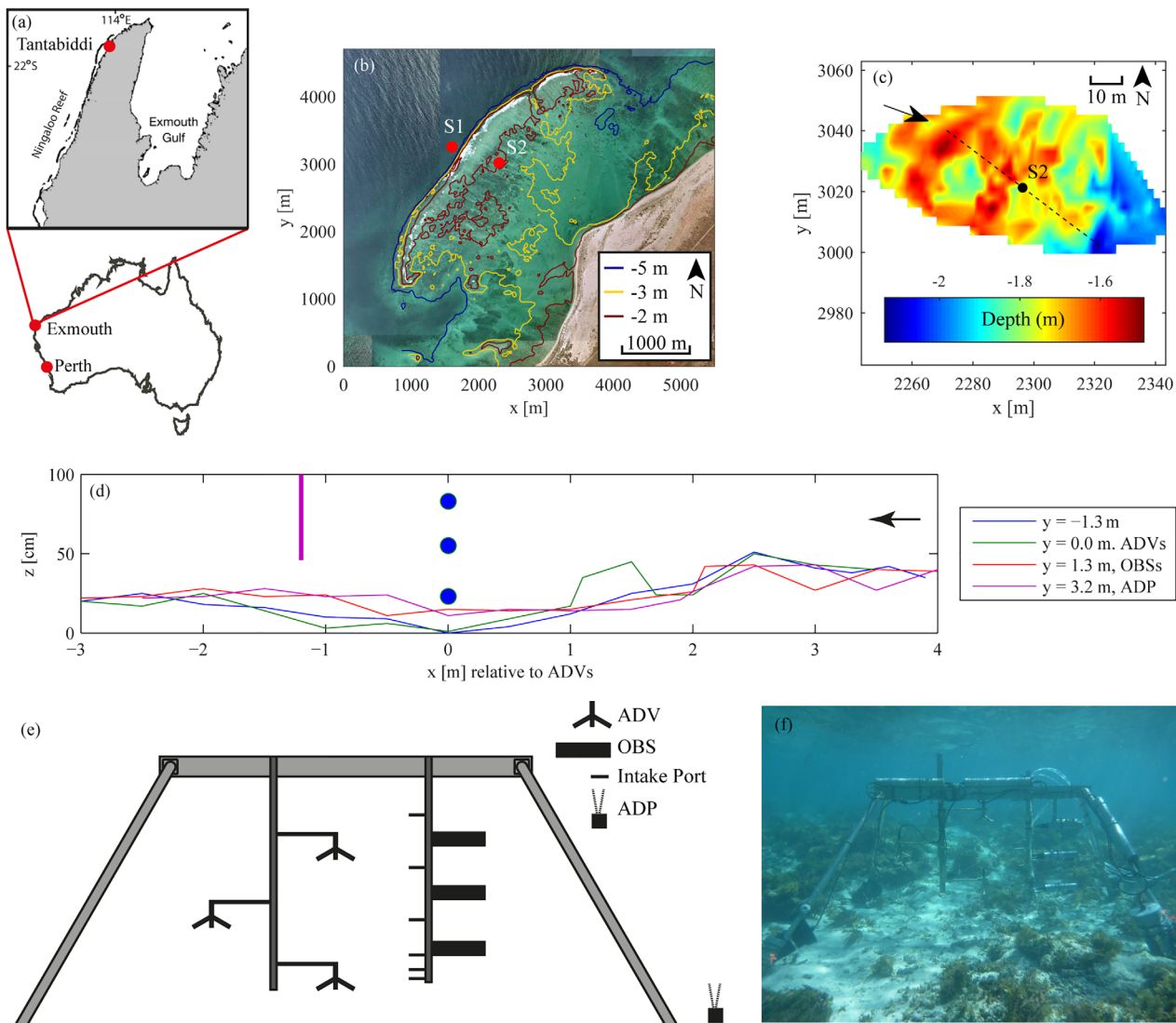


Figure 2. (a) The location of Tantabiddi within Ningaloo Reef in northern Western Australia. (b) An aerial view of the site in site (origin: 21.89248°S, 113.96203°E) with the location of the instruments relevant to this study and key contours indicated. (c) Interpolated sonar bathymetry around the high-resolution sampling site on the reef flat relative to the mean water level, with the mean flow direction indicated. The dashed line indicates the cross-reef direction. (d) Bathymetry transects measured perpendicular to the sawhorse frame from south to north and relative to the location of the vertical ADV array (blue dots). The vertical line indicates the vertical range of the ADP profiler within the vertical scale of the figure. The arrow denotes the mean flow direction during the experiment. (e) Schematic illustration of the sawhorse frame deployed in the experiment and (f) an underwater image of the site with the deployed instrumentation.

In an $\sim 40 \text{ m} \times 40 \text{ m}$ region surrounding the sawhorse frame, a fine-scale topographic survey was used to quantify the bottom roughness. The bathymetry was measured (Figure 2c) with single-beam acoustic sonar (Humminbird 798c) and supplemented with four manually measured roughness transects spaced at $\sim 1.5 \text{ m}$ horizontally (Figure 2d). Each manual transect was defined by an 8 m wire that was tensioned and leveled. The distance between the bed and the wire was measured every 1 m horizontally with 1 cm vertical resolution. The roughness survey indicates that the coverage in benthic roughness varied and consequently the roughness characteristics were somewhat patchy with slightly larger roughness elements (in vertical dimension) located upstream of the sampling site.

3.3. Data Analysis

3.3.1. Hydrodynamic Data

Offshore wave conditions (wave height, period, and direction) were measured on the forereef (S1) using a Nortek acoustic wave and current meter (AWAC) with acoustic surface tracking (AST); whereas wave conditions on the reef flat were obtained from pressure time series converted to surface elevations using linear

Table 2. Instrument Site Information and Sampling Configuration^a

Site and Depth	Instrument	Sampling Information
S1 (forereef ~10.5 m)	Nortek AWAC	1 Hz with 2048 s burst every 3600 s; current profile every 5 min, 30 bins at 0.5 m; velocity sample height: 1.04 m
	RBRVirtuoso D	Continuous sampling at 1 Hz; pressure sample height: 0.2 m
S2 (reef flat ~1.5 m)	Nortek ADV	8 Hz with 2048 s burst every 3600 s; velocity sample height: 0.23 m, 0.53 m and 0.85 m.
	Nortek ADP-HR	Continuous 1 Hz current profile, 31 cells at 25 mm, velocity sample height: 0.22 m; pressure sample height: 0.07 m
	Wetlabs FLNTU Suction samples	0.29 Hz with 462 samples every 3600 s; sample heights: 0.37, 0.64, 0.90 m Hourly during daylight; SSC sample heights: 0.22, 0.27, 0.34, 0.51, 0.76, 1.02 m

^aSamples heights are relative to the seabed.

wave theory. From the wave spectra, the root-mean-squared (RMS) wave-heights for the shorter-period (5–25 s) sea-swell waves ($H_{rms,sw}$) and longer period (25–250 s) infragravity ($H_{rms,ig}$) waves, as well as the peak period (T_p), were calculated through integration of the energy within these respective bands.

The raw ADV and ADP velocity measurements were initially filtered based on low signal correlations (<60%) before velocity spikes (e.g., caused by bubbles or debris in the sample volume) were removed using a kernel-based despiking algorithm [Goring and Nikora, 2002]. The direction of the waves and currents was computed separately so that the angle between the waves and currents could be considered in the calculation of the bed shear stresses imposed by the wave-current boundary layer. For each 15 min burst of data, the mean current (\bar{u}) speed and direction were computed. The reef flat free-stream velocity (\bar{u}_∞) was defined as the depth-averaged current speed of the top five ADP cells unaffected by the free surface (i.e., roughly 0.7–0.8 m above the sediment bed). The mean current vector was then removed from each velocity record and the (residual) oscillatory velocity data rotated into a coordinate system that maximized the velocity variance along the primary axis. In this coordinate system, the wave (\tilde{u}) and RMS velocities (\tilde{u}_{rms}) were determined.

Across a range of conditions, a logarithmic velocity profile was consistently observed within a region approximately 0.5–0.8 m (~12 data points) above the bed (Figure 3). Above the upper height, the flow profile at times deviated from a logarithmic form as it approached a free-stream velocity; below the lower height, the flow profile was often inflected, consistent with a canopy flow (e.g., Figure 1). This transition toward the in-canopy flow occurred at an elevation that was comparable to the measured height of the roughness near the site (~20–40 cm). To determine the mean shear velocity above the roughness sublayer ($u_{*,m,rough}$) for the combined wave-current flow (see section 2.3), a least squares best fit of equation (1) against the time-averaged 15 min bursts of the ADP data within the logarithmic region (0.5–0.8 m above bed) was conducted. To ensure a robust logarithmic profile existed, we only retained estimates of $u_{*,m,rough}$ from profiles with a $R^2 > 0.95$, with the vast majority (~90%) of the bursts satisfying this criterion. The boundary layer theory of Grant and Madsen [1979] and the implementation described by Madsen [1994] was used to calculate $u_{*,max,rough}$. We used \bar{u} and u_{rms} measured above the logarithmic layer ($z=0.8$) and the z_{0a} from the logarithmic fit to define an equivalent Nikuradse roughness (i.e., $k_N=30z_{0a}$).

Estimates of $u_{*,m,rough}$ were compared to those calculated from the turbulence data measured by the ADVs. Here we further separated the measured horizontal and vertical data into wave (\tilde{u} and \tilde{w}) and turbulent velocity (u' and w') components. We used data from the top and middle ADVs for this decomposition, whereby the turbulent motion was obtained by removing correlated motions between the two instruments (i.e., waves) [Shaw and Trowbridge, 2001]. The mean shear velocity enhanced by waves and currents was then determined from the Reynolds stresses ($u_{*,m,rough}^2 = -\bar{u}'\bar{w}'$) at the middle ADV ($z=0.5$ m). At this elevation, the Reynolds stresses are expected to be slightly below the inertial sublayer (logarithmic) region and representative of the shear velocity just above the roughness elements.

The bottom ADV located below the roughness height was of poorer quality, so it was only used to evaluate the mean current and wave velocities, but not to obtain direct estimates of the Reynolds stresses. To estimate the magnitude of the mean ($u_{*,m,bed}$) and maximum wave-current shear velocity ($u_{*,max,bed}$) at the sediment

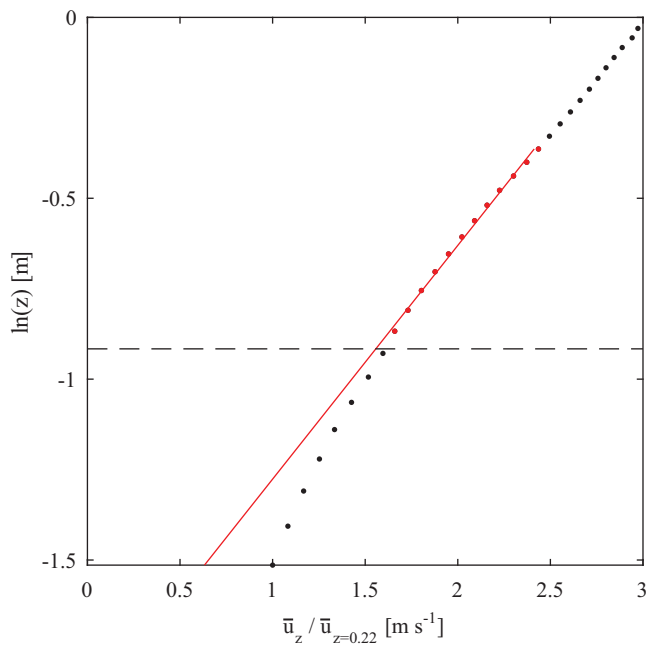


Figure 3. A logarithmic fit of equation (1) (red) to the mean of the individual 15 min time-averaged velocity profiles measured during the experiment. The velocity measurements are normalized by the velocity measurement closest to the bed. The red dots denote the points used in the fit and the horizontal dashed line indicates 0.4 m above the bed, the approximate height of the roughness observed at the site.

imaged under a microscope to obtain ~ 50 evenly spaced images of the filter surface that were obtained with an accuracy of 2 pixels: 1 μm . For each image, the sediment grains were manually identified under a microscope and their location recorded on the image. A Canny edge detection algorithm [Canny, 1986] was then used in MATLAB to detect the edge of the particles in each image based on local maxima of the image intensity gradient. The largest and smallest dimension of the irregularly shape particles was manually identified in order to determine the size of the particles. Particles with dimensions $< 50 \mu\text{m}$ were omitted, as it was often difficult to identify a clearly defined particle boundary and thus these particles could not be reliably measured.

To relate the suspended sediment grain size distribution to the shear stresses above and within the canopy, we determined the equivalent grain size that could be suspended by a given shear velocity based on the downward particle fall velocity (w_s):

$$\frac{u_*}{w_s} = \alpha \quad (3)$$

where α represents the different stages of suspension and ranges from bursts of sediment in suspension when $\alpha \leq 1$ to fully developed suspension when $\alpha \gg 1$ [Bagnold, 1966; Van Rijn, 1984]. Note that this ratio is related to the inverse of the Rouse number. We set $\alpha=1$ based on the following arguments: (1) For a specific grain size to be suspended from the bed it must have experienced a shear stress that was sufficient to enable it to be mobilized from the bed. (2) For the range of sediment grain sizes measured in suspension in this experiment, once these grains are mobilized they (theoretically) directly enter a state of suspension [e.g., Bagnold, 1966; Francis, 1973]. (3) The state of suspension (i.e., whether sediment is in a burst or fully developed suspension) is not relevant for the current analysis. Here we use the Soulsby [1997] formulation to estimate w_s as:

$$w_s = \frac{\nu}{D} \left(\sqrt{10.36^2 + 1.049 D_*^3} - 10.36 \right) \quad (4)$$

where ν is the kinematic viscosity of the water ($9.35 \times 10^{-7} \text{ m}^2 \text{s}^{-1}$), D is the particle size of interest, and D_* is the dimensionless grain size ($D_* = (g(s-1)/\nu^2)^{1/3} D$) with g the gravitational acceleration constant

bed (at the base of the canopy, Figure 1d), we again used the approach described by Madsen [1994] but now with the velocities measured by the bottom ADV. For this flow within the canopy, the roughness was defined with the Nikuradse sand grain roughness ($k_N = 2.5 D_{50}$) determined from the median bed grain size measured at the bed level between the roughness elements ($D_{50} \approx 240 \mu\text{m}$, Figure 8b).

3.3.2. Suspended Sediment Grain Sizes and Concentrations

Suspended sediment grain sizes and concentrations were determined from suction samples at hourly intervals during daylight hours. The water samples were collected with peristaltic pumps via intake ports located perpendicular to the dominant cross-reef flow direction [Bosman et al., 1987] and stored in 2 L bottles. The samples were vacuum filtered onto preweighed membrane filters (Whatman ME27, 0.8 μm), dried (75°C for 24 h) and weighed in order to calculate SSCs. The dried filters were then

Table 3. Calibration Parameters Used for the Linear Conversion of the ADP and OBS Backscatter Data (B_k) to Suspended Sediment Concentrations (SSC)^a

$Z_{\text{instrument}}^{\text{b}}$ (m)	Z_{port} (m)	Calibration Equation (mg L ⁻¹)	R^2	p	n
<i>ADP</i>					
0.52	0.51	$SSC = 0.052 B_k - 2.68$	0.61	<0.001	35
0.77	0.76	$SSC = 0.062 B_k - 3.25$	0.64	<0.001	31
1.02	1.01	$SSC = 0.067 B_k - 3.53$	0.61	<0.001	28
<i>OBS</i>					
0.37	0.34	$SSC = -0.95 B_k + 6.59$	0.76	<0.001	10
0.64	0.76	$SSC = -0.64 B_k + 4.72$	0.73	<0.001	11
0.90	1.02	$SSC = -2.73 B_k + 9.52$	0.51	0.109	5

^aFor the ADP, the nearest cell to the suction port was used in the calibration while the nearest port to the OBS sample cell was used for the OBS calibration.

^bCell height corrected for difference in bathymetry between suction sample ports and ADP which is estimated to be ~0.20 m.

and s is the ratio of the carbonate sediment grain density ($\rho_s = 2600 \text{ kg m}^{-3}$) estimated by gravitational displacement [Cuttler et al., 2015] to water density ($\rho_w = 1026 \text{ kg m}^{-3}$) from sediment samples obtained at the site.

The OBS and ADP backscatter data were calibrated with the SSC measurements obtained by suction sampling. The known SSCs obtained through filtration were related via linear regression (Table 3) to the measured backscatter, time-averaged over the duration when the suction samples were obtained. For the OBS instruments, the suction sample intake port that was closest (vertically) to the optical measurement elevation was used in the calibration, whereas for the ADP data (corrected for acoustic decay, e.g., Ha et al. [2011]) we related three measurement cells to their adjacent intake ports and then applied the mean linear-fit equation to the data. The root-mean-squared error (RMSE) of the calibrated OBS and ADP backscatter was $\sim 0.20 \text{ mg L}^{-1}$ for all instruments, except for the middle OBS that was slightly lower ($\sim 0.13 \text{ mg L}^{-1}$); these errors were much smaller than the typical measurements that ranged from $0.5\text{--}8 \text{ mg L}^{-1}$ (section 4.3.2). The calibrated backscatter therefore provided a reasonably accurate measure of SSCs in this experiment due to the narrow distribution of fine sediment at low concentration that we observed (see below) [e.g., Francois and Garrison, 1982; Richards et al., 1996].

4. Results

4.1. Hydrodynamic Conditions

During the first part of the experiment (1–5 August 2013), the offshore RMS wave heights ($H_{rms,sw}$) measured on the fore reef at S1 were small and relatively consistent ($\sim 0.5\text{--}0.8 \text{ m}$, Figure 4b). Two larger swell events (6–8 and 9–11 August 2013) occurred during the latter part of the experiment, with maximum wave heights reaching $\sim 1.7 \text{ m}$ during both events. Peak periods (T_p) ranged from 12 s during lower wave conditions to up to 19 s during the larger swell events (Figure 4b). There was a large reduction in sea-swell wave heights ($H_{rms,sw}$) on the reef flat at S2 (Figure 4d). Variations in the water depth, predominantly driven by the tide (Figures 4a and 4c), strongly modulated $H_{rms,sw}$ on the reef flat through depth-limited wave breaking (Figure 4d); however, the infragravity wave heights ($H_{rms,ig}$) were not strongly modulated by the water depth, responding much more to the offshore $H_{rms,sw}$. As a consequence, the $H_{rms,sw}$ on the reef flat were larger than $H_{rms,ig}$ during high tide, but were similar or smaller than $H_{rms,ig}$ at low tide during the larger swell events.

Mean free-stream current velocities (\bar{u}_∞) on the reef flat varied in response to the offshore wave conditions ($\sim 0.05\text{--}0.45 \text{ m s}^{-1}$) as a result of the dominant wave-driven currents on the reef flat, with only small variability associated with the tides (typically by $\pm 0.05 \text{ m s}^{-1}$) (Figure 4e). Thus, during the first part of the experiment the flows tended to be dominated by wave orbital velocities ($\bar{u}_\infty/\tilde{u}_{rms} < 1$, where \tilde{u}_{rms} is the RMS value of the wave velocity, Figure 4f). At low tide, the combined effect of smaller waves and the relative increase in mean flow resulted in mixed wave-current conditions ($\bar{u}_\infty/\tilde{u}_{rms} \sim 1$). During the larger offshore swell events, due to the depth-limitation of wave heights on the reef flat and stronger wave-driven mean currents, the reef flat became current-dominated ($\bar{u}_\infty/\tilde{u}_{rms} > 1$) over much of this period.

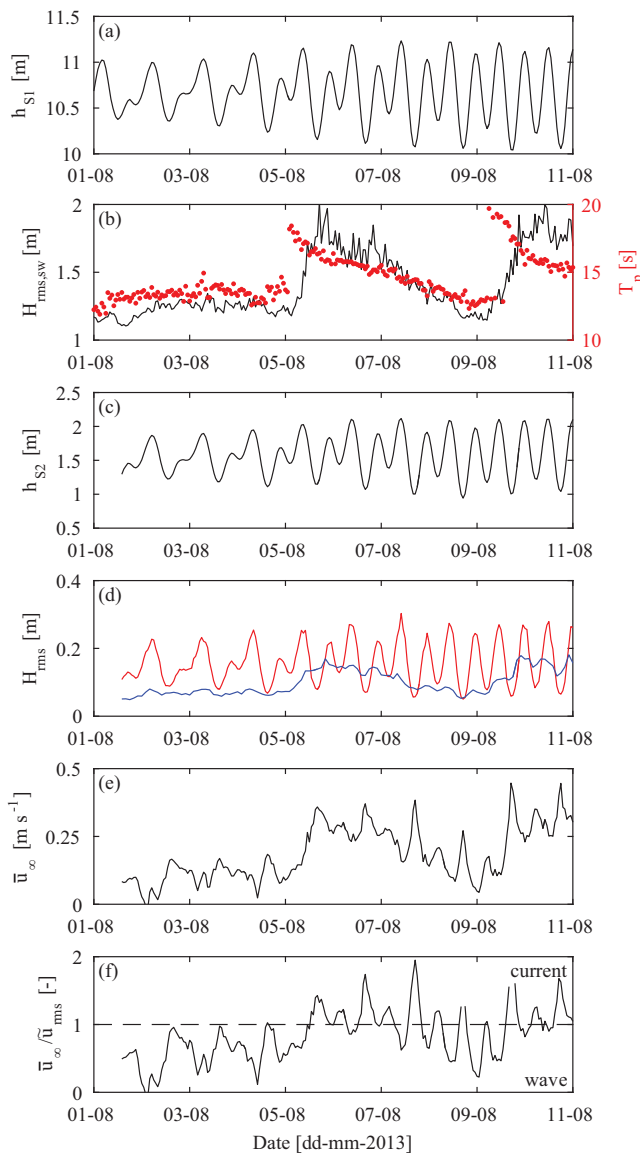


Figure 4. The forereef S1 (a) water depth and (b) swell root-mean-squared (RMS) wave height $H_{rms,sw}$ and peak wave period T_p , along with the intensive sampling reef flat S2 site, (c) water depth, (d) sea-swell ($H_{rms,sw}$, red) and infragravity ($H_{rms,ig}$, blue) RMS wave height, the (e) free-stream velocity defined as the depth-averaged velocity above the identified logarithmic region and (f) the relative importance of the free-stream mean flow versus the RMS wave-induced flow. The dashed horizontal line indicates the threshold above which the conditions are current-dominated.

$\pm 10\text{--}20^\circ$, thus changes in upstream roughness may also affect the estimated shear stress and could account for some of the scatter observed.

4.2.2. Within the Roughness

Within the roughness (canopy) region, there was greater attenuation of the mean current relative to free-stream values when compared to the wave velocities (Figure 6). In this near-bed region, the currents were generally reduced to only $\sim 25\%$ of the free-stream velocity (Figures 6a and 6b), whereas the RMS wave velocities generally remained $\sim 75\%$ of the free-stream values (Figures 6c and 6d).

The estimated mean shear velocity imposed on the underlying sediment bed ($u_{*,m,bed}$) was approximately four times smaller than the mean shear velocity at the top of the roughness ($u_{*,m,rough}$, Figure 7a). Similarly, the maximum wave-induced shear velocity was much larger at the top of the canopy ($u_{*,max,rough}$) than at

4.2. Flow Structure and Turbulent Stresses

4.2.1. Above the Roughness

The mean current profile above the roughness was consistently logarithmic over the full range of current and wave conditions ($\sim 90\%$ of the data conformed to equation (1) with an acceptance threshold of $R^2 > 0.95$). The mean shear velocities ($u_{*,m,rough}$) estimated from equation (1) usually agreed well with those derived from the ADV-derived Reynolds stresses throughout the experiment (Figure 5a). When these $u_{*,m,rough}$ values are converted to a bottom friction coefficient ($C_f = u_{*,m,rough}^2 / \bar{u}_\infty^2$), the mean value for the duration of the experiment was 0.035 (standard deviation 0.012). These C_f are within the range ($0(0.01)$) that are typically reported for other reef flats [e.g., Lowe and Falter, 2015, for a review]. This suggests that the dynamics observed in this experiment are unlikely to be unique to this site.

Values of $u_{*,m,rough}$ estimated from the log-fitting increased approximately linearly with mean current speed and were maximum when $\bar{u}_\infty \sim 0.3 \text{ m s}^{-1}$; however, appeared to decrease slightly for the largest values of \bar{u}_∞ , albeit with more scatter (Figure 5b). Furthermore, for a given value of \bar{u}_∞ , $u_{*,m,rough}$ increased as the hydraulic roughness (z_{0a}) increased. This increase in z_{0a} occurred as the conditions became more wave-dominated (Figure 5c). The increase in both $u_{*,m,rough}$ and z_{0a} under stronger wave conditions is consistent with the enhancement of the mean bottom stresses (and apparent bottom roughness) by waves. We note that the current direction varied slightly throughout the experiment (only by

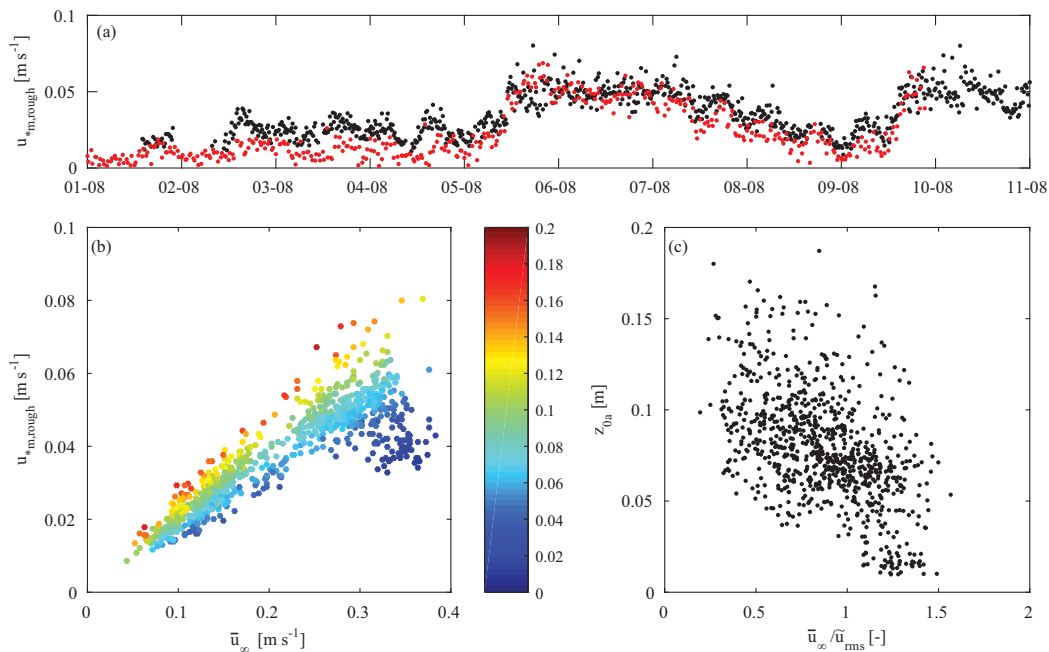


Figure 5. (a) The shear velocity ($u_{*m,rough}$) estimated from the middle ADV Reynolds stress (red) compared with the $u_{*m,rough}$ estimated from the ADP time-averaged velocity profiles with equation (1) (black). (b) $u_{*m,rough}$ as a function of the free-stream velocity (\bar{u}_∞). The color bar denotes values of the roughness length scale (z_{0a}). (d) The roughness length scale (z_{0a}) as a function of the current-wave ratio ($\bar{u}_\infty / \bar{u}_{rms}$). Note that all values in Figures 5b and 5c are based on estimates from the ADP data.

the bed ($u_{*max,bed}$, Figure 7b). When the shear velocities at the bed were compared, $u_{*max,bed}$ was approximately twice as large as $u_{*m,bed}$ (Figure 7c). We note here that while there is some spatial variability in the velocity measured by the ADV and ADP (Figure 6), likely due to fine-scale spatial variations in the roughness, this velocity variability is small. Thus, any differences in shear stresses estimated by the ADV and ADP will also be small, relative to the large vertical differences in the shear stress (i.e., at the bed and at the top of the canopy).

4.3. Suspended Sediment

4.3.1. Grain Size Distributions

The grain size distributions obtained from the suction samples were similar across the various samples analyzed in the experiment. Although a small number of larger grains were identified in the microscope analysis, ~50% of the grains were within the range of 60–85 µm, with a typical median grain size (D_{50}) of ~70 µm (Figure 8a). We expect there to be some material that is finer than 50 µm (the lower limit of the analysis) that would shift the median slightly finer; however, we only observed a very small amount of material at 50 µm, so we do expect this contribution to affect the results. The maximum contribution of the larger grains (>150 µm) was consistently less than 10% for each of the analyzed samples. This is in contrast to the distribution of the bed sediment at this site, which was dominated by much coarser sediment mostly ranging from ~150 to 500 µm ($D_{50} = 240$ µm) (Figure 8b).

The $u_{*m,rough}$ was predicted to be well-beyond what was needed to maintain much of the bed sediment in suspension, as determined from the fall velocity in equation (3) (red solid line, Figure 8b); however, these larger grain sizes were notably absent from the water column (Figure 8a). The absence of these large size fractions in suspension indicates that the shear stress applied to the sediment was substantially smaller than the mean shear at the top of the roughness. This discrepancy is even greater if we consider $u_{*max,rough}$, which would be capable of suspending sediment up to $D_{50} = 550$ –1000 µm (off the scale in Figure 8a).

The grain sizes observed in the water column were much closer to the equivalent grain size that could be maintained in suspension by $u_{*m,bed}$ (Figure 8a, blue solid line). However, we also note that a substantial

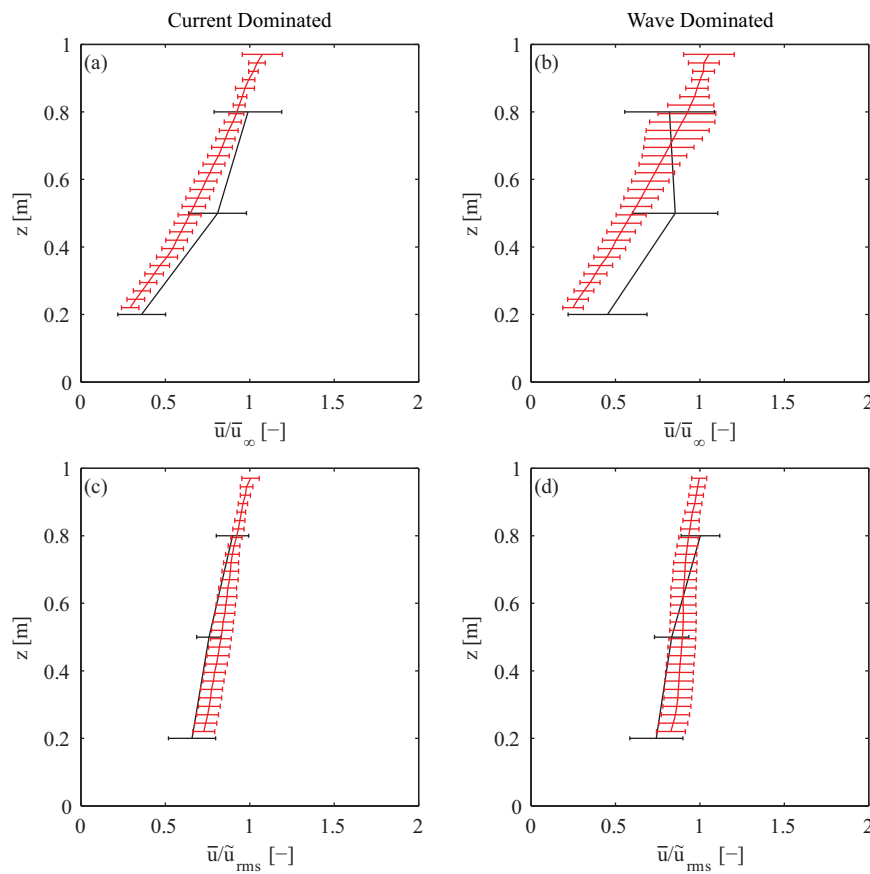


Figure 6. Mean current (\bar{u}) profiles for (a) current-dominated and (b) wave-dominated conditions along with RMS velocity (\bar{u}_{rms}) profiles for (c) current-dominated and (d) wave-dominated conditions. For all profiles, the ADP measurements are shown in red and the ADV measurements are shown in black with the horizontal error bars denoting ± 1 standard deviation. The mean current profiles have been normalized by the free-stream current (\bar{u}_∞) and the RMS velocity profiles have been normalized by \bar{u}_{rms} above the roughness.

proportion of the suspended sediment distribution remained above this estimate. If the enhanced shear velocity due to waves ($u_{*,max,bed}$) is considered, the range of grain sizes that could be maintained in suspension encompasses almost the entire suspended sediment distribution that was observed (blue dashed line, Figure 8a).

The relationship between the shear velocities and the measured SSC samples was also consistent throughout the duration of the experiment: $u_{*,m,rough}$ was sufficient to suspend the observed D_{50} that was in suspension and the seabed D_{50} during the swell events; $u_{*,max,rough}$ was consistently large enough to suspend the

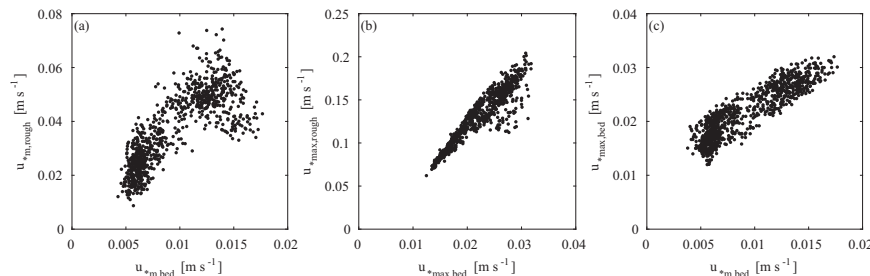


Figure 7. (a) The mean shear velocity at the bed ($u_{*,m,bed}$) compared to the mean shear velocity at the top of the roughness ($u_{*,m,rough}$). (b) The maximum shear velocity at the bed ($u_{*,max,bed}$) compared to the maximum shear velocity at the top of the roughness ($u_{*,max,rough}$). (c) $u_{*,m,bed}$ compared to $u_{*,max,bed}$.

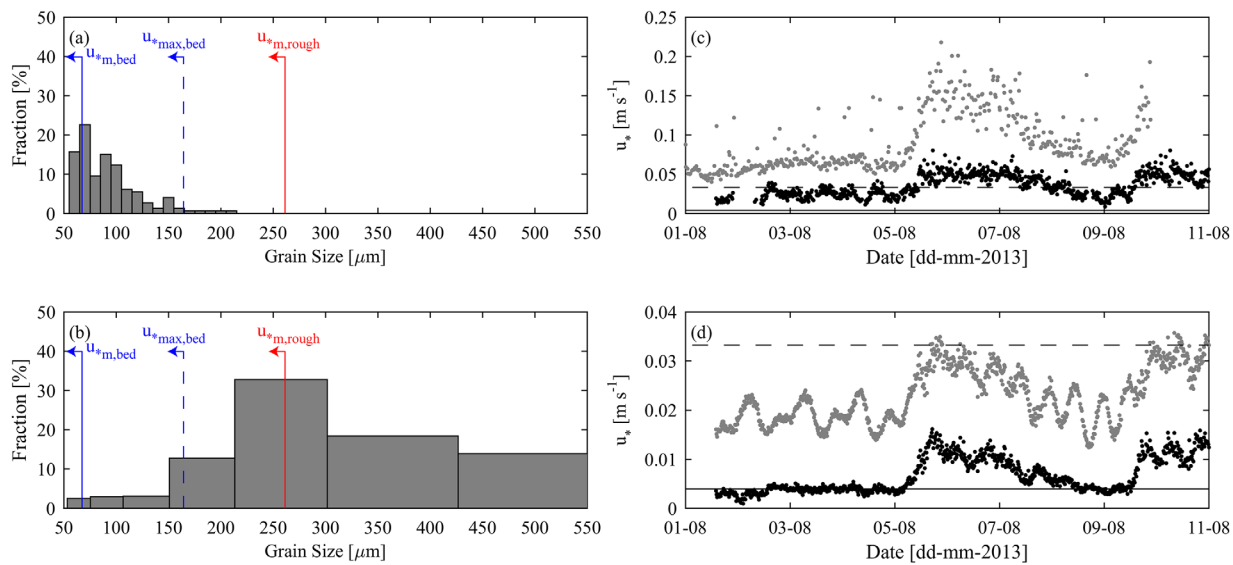


Figure 8. Grain size distribution from (a) suction samples obtained at the port closest to the bed ($z = 0.23$ m) and (b) determined from a bed surface sample obtained on the reef flat at S2. The histogram in (a) represents the distribution from a sample obtained at 15:00 on 2 August 2013 (local time). The vertical lines indicate the equivalent sediment diameter that could be suspended by the mean ($u_{*,m,bed}$) (solid blue) and maximum ($u_{*,max,bed}$) (dashed blue) wave-induced bed shear velocities, and the mean shear velocity ($u_{*,m,rough}$) (solid red) at the top of the roughness (canopy) layer. Note that the equivalent grain size that could be maintained in suspension by the maximum wave-induced shear velocity ($u_{*,max,rough}$) at the top of the roughness layer is $\sim 830 \mu\text{m}$ and is not indicated on the figure. The maximum (gray) and mean (black) shear velocity at the top of the roughness layer (c) and within the roughness layer (d) are shown for the entire experiment. The horizontal dashed line indicates the shear velocity required to suspend the median grain size observed in the suction samples.

seabed D_{50} (Figure 8c). Within the roughness, $u_{*,m,bed}$ alone was sufficient to suspend the observed D_{50} that was in suspension, however the addition of the wave-component of the enhanced bed stress is clearly evident throughout the time series but remained insufficient (except at the peak of the swell events) to suspend the seabed D_{50} (Figure 8d).

4.3.2. Sediment Concentrations and Fluxes

The calibrated ADP and OBS backscatter data were consistent with the SSCs measured directly by suction sampling throughout the experiment (Figures 9a–9c). Early in the experiment when the waves were low (1–6 August), the SSC varied from $\sim 0.5 \text{ mg L}^{-1}$ at low tide to $\sim 2\text{--}3 \text{ mg L}^{-1}$ at high tide. During the larger swell events spanning 5–8 and 9–12 August, the SSCs were consistently higher and peaked at $\sim 8 \text{ mg L}^{-1}$ but continued to vary with tidal phase.

The form of the concentration profile defined by the ADP backscatter and the suction samples was grouped according to four hydrodynamic conditions: (I) low offshore waves and rising tide (Figure 9d), (II) low offshore waves and falling tide (Figure 9e), (III) high offshore waves and rising tide (Figure 9f), and (IV) high offshore waves and falling tide (Figure 9g). For condition (I), no direct suction samples were obtained during the field experiment, so only profiles derived from the calibrated ADP are shown. For each of the remaining conditions, the time-averaged SSC profile inferred from the calibrated ADP backscatter was comparable in structure to the mean SSC profile described by the suction samples. Each concentration profile exhibited similar features: near the bed, the concentration was low but increased slightly with height above the bed; then above the roughness sublayer, a near constant concentration was observed. There was a very strong relationship between the depth-integrated SSC within the roughness ($z=0.2\text{--}0.4$ m) and both $u_{*,m,bed}$ and $u_{*,max,bed}$ (Figure 10). However, no clear relationship was observed when $u_{*,m,bed}$ was small ($<0.005 \text{ m s}^{-1}$), i.e., when the wave contribution was also small.

5. Discussion

Few studies have directly measured sediment transport over large roughness, especially in a natural field setting. However, the presence of roughness has been thought to decrease sediment transport rates through the attenuation of velocity and turbulence within the roughness sublayer (i.e., the canopy) in

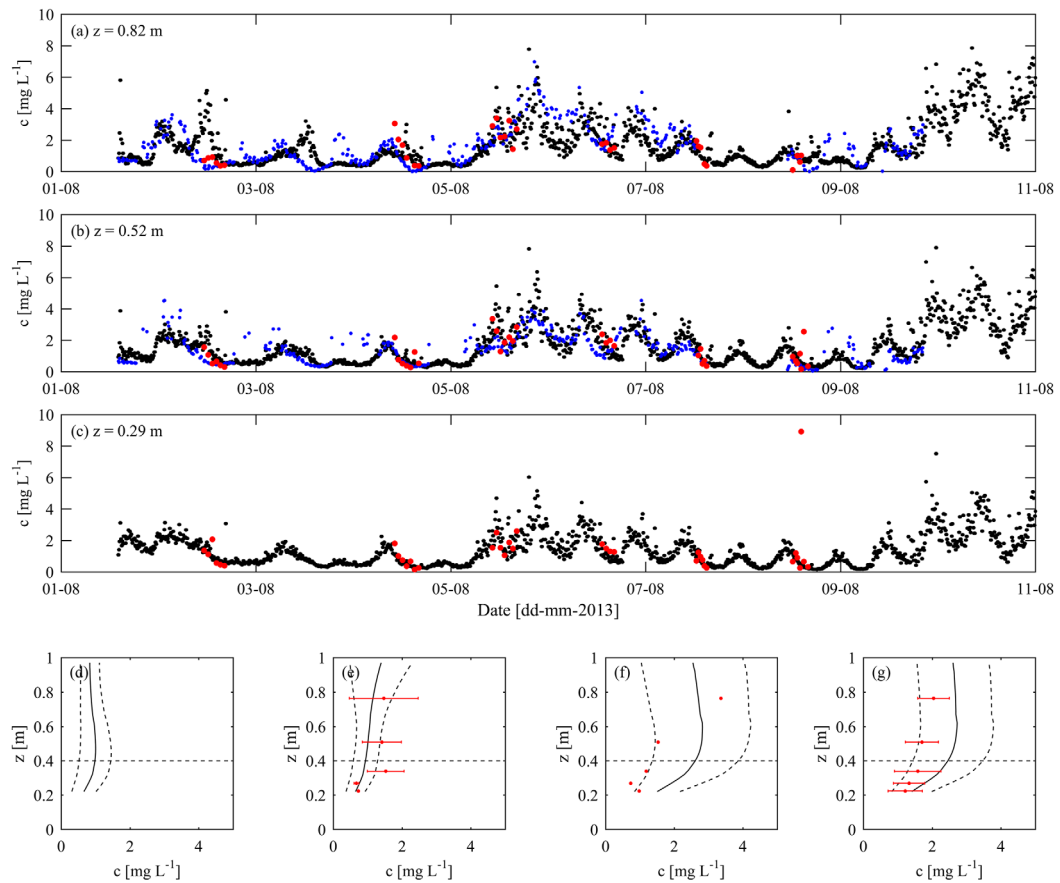


Figure 9. Suspended sediment concentration (SSC) time series measured at (a) $z = 0.82 \text{ m}$, (b) $z = 0.52 \text{ m}$, and (c) $z = 0.29 \text{ m}$ above the bed. The black dots indicate the SSC estimated from the calibrated ADP, blue dots the OBS backscatter and the red dots indicate the directly measured SSC from the suction samples. The mean SSC profile measured by the calibrated ADP (black line) and directly from the suction samples (red dots) for the forereef conditions: (d) low waves and rising tide (note: no suction samples were obtained for this condition), (e) low waves and falling tide, (f) high waves and rising tide, and (g) high waves and falling tide. The vertical dotted lines and error bars indicate one standard deviation in the measured data. The horizontal dotted line indicates the approximate height of the roughness.

terrestrial [e.g., Prosser *et al.*, 1995], riverine [e.g., Neary *et al.*, 2011], and estuarine [e.g., Ward *et al.*, 1984] environments. Of the studies that have specifically considered sediment transport within canopies, most have been from unidirectional laboratory-based experiments that only consider bulk sediment transport rates from changes in the bed morphology or sediment traps, with most attention also focused on emergent canopies [e.g., Baptist, 2005; Jordanova and James, 2003; Le Bouteiller and Venditti, 2015; Widdows *et al.*, 2008]. This present study provides new quantitative insight into how suspended sediment grain sizes, SSCs, and SSFs are modified by the presence of submerged roughness on a coral reef flat that is subject to both waves and currents.

Typically, field studies conducted on reefs have empirically related sediment transport rates to shear velocities estimated from hydrodynamics measurements above the roughness (i.e., a measure of the total flow resistance, including the effect of form drag) [e.g., Ogston *et al.*, 2004; Presto *et al.*, 2006]. In this present study, we make a direct connection between the observed suspended sediment grain sizes and the reduced hydrodynamic forces present at the sediment bed at the base of the immobile roughness. From these suspended sediment observations, we then determined the shear velocity at the bed required to suspend the observed sediment. Both the mean ($u_{*m,rough}$) and maximum ($u_{*max,rough}$) shear velocities determined from the hydrodynamics above the roughness layer were approximately an order of magnitude larger than those required to suspend the observed grain sizes within the bed, despite none of this material being observed in suspension. Therefore, $u_{*m,rough}$ and $u_{*max,rough}$ were poor predictors of the actual sediment grain sizes that were observed in suspension, whereas estimates obtained

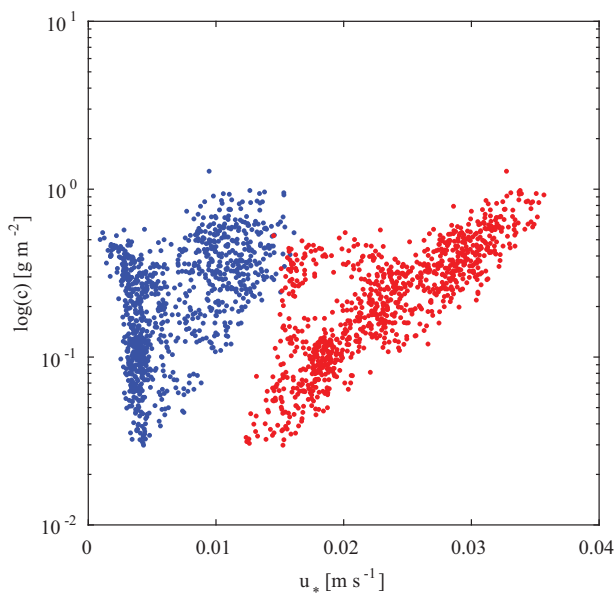


Figure 10. Depth-integrated suspended sediment concentration (SSC) within the roughness ($z = 0.2\text{--}0.4\text{ m}$) determined from the ADP backscatter compared to the mean bed shear velocity (blue) and maximum bed shear velocity (red).

using the reduced bed friction velocities ($u_{*m,bed}$ and $u_{*max,bed}$) were much more consistent with the observations.

Although some studies have previously considered how large immobile roughness on the bed can reduce overall bulk sediment transport rates [e.g., Bouma et al., 2007; Le Bouteiller and Venditti, 2015], how this roughness influences suspended sediment transport has remained poorly understood. In the present study, $u_{*m,bed}$ was still not large enough to explain the suspended sediment D_{50} . However, when $u_{*max,bed}$ was considered, almost the entire range of the observed suspended sediment grain sizes were predicted to be in suspension. This suggests that the range and relative proportions of grain sizes in suspension are explained by the wave orbital velocities within the roughness (canopy), and also differences between how wave and current motions dynamically interact within a canopy.

5.1. The Influence of Roughness on Suspended Sediment Concentration Profiles

The observation of persistently elevated sediment concentrations near the top of the roughness, relative to values near the bed, contrasts with a multitude of observations in other environments (e.g., beaches and rivers) of monotonically decreasing concentration with height above the bed. While this profile may at first appear counter-intuitive, the hydrodynamic influence of the large roughness provides a possible explanation (explored in this section) for the development of this profile.

In flow over an erodible bed for which the ratio w_s/u_* is small, sediment will be entrained from the bed into the water column, where it will be transported (advection) as suspended sediment. At equilibrium, sediment suspension balances sediment deposition; otherwise, the sediment concentration will vary with streamwise distance until an equilibrium profile is attained. The distribution of sediment in suspension is typically modeled as a vertical diffusive process, which can be described by the advection-diffusion equation:

$$\underbrace{\frac{\partial(uc)}{\partial x}}_1 - \underbrace{\frac{\partial(w_s c)}{\partial z}}_2 - \underbrace{\frac{\partial}{\partial z} \left(\varepsilon_s \frac{\partial c}{\partial z} \right)}_3 = 0 \quad (5)$$

In equation (5), Term 1 describes the horizontal advection of sediment, Term 2 gravitational settling, and Term 3 the vertical diffusion of sediment. Here ε_s is the sediment mixing (diffusion) parameter, which can be approximated (in various forms) as a function of the turbulent eddy viscosity (v_t) or u_* [e.g., Van Rijn, 1984].

The development of suspended sediment concentration profiles over erodible beds with and without roughness is obtained by solving equation (5) with an upwind numerical scheme. We consider the case of a uniform sediment concentration upstream of the roughness ($c_{x=0}$) due to, e.g., wave breaking in an upstream surf zone. To solve equation (5), two boundary conditions are required: (i) at the upper boundary (the free surface) there is zero vertical flux, and (ii) at the bed ($z=0$), the upward diffusive flux balances gravitational settling (i.e., $w_s c = -\varepsilon_s \partial c / \partial z$). Typically, a near-bed reference concentration (c_0) is used to specify this bottom boundary condition. Many formulations have been developed for c_0 , most of which functionally depend on the shear stress applied to the sediment bed [e.g., Lee et al., 2004; Smith and McLean, 1977]. Here we specified a spatially constant (i.e., in the streamwise direction x) c_0 using the formulation proposed by Lee et al. [2004]:

$$c_0 = A \left[\theta \frac{u_*}{W_s} \right]^B \quad (6)$$

where c_0 is defined at a reference height $z_{ref}=0.01$ m above the bed, θ is the grain roughness Shields parameter, and u_* is the shear velocity at the sediment bed. We use $A = 2.58$ and $B = 1.45$ for the two empirically derived constants, but recognize that there is some uncertainty around these values [Lee et al., 2004].

For comparison, we first determine the concentration profile over a bare erodible bed (i.e., without roughness). Typical values of the uniform mean current ($\bar{u}=0.3$ m s $^{-1}$), uniform grain size in suspension (70 μm) and bed friction velocity ($u_*=0.08$ m s $^{-1}$) are used. The sediment diffusivity (ε_s) is assumed to increase linearly with height above the bed (i.e., $\varepsilon_s = v_t = \kappa u_{*\max,rough} z$, Figure 11a). With this diffusivity profile, the initially uniform concentration profile, which in this example we initialize with c_0 , evolves downstream to form a classic exponentially decaying profile above the bed (Figure 11b).

In this study, we typically observed a fourfold difference between $u_{*\max,rough}$ and $u_{*\max,bed}$ due to the large bottom roughness. The presence of large roughness therefore has two important modifications to the solution to equation (5). First, τ_{bed} is reduced and consequently so is c_0 . For comparison with the bare bed case, we assume the same maximum value of u_* here at the height of the roughness (i.e., $u_{*\max,rough}=0.08$ m s $^{-1}$) and a reduced value for $u_{*\max,bed}$ (which is used in equation (6) to determine c_0) of 0.02 m s $^{-1}$; as a consequence c_0 is also lower in the presence of the roughness. Second, flume experiments have shown that in unidirectional flow over large roughness, the turbulent diffusivity decreases linearly from a maximum value near the top of the roughness to a diminished value deep within the roughness [e.g., Ackerman and Okubo, 1993; Ghisalberti, 2007; Ghisalberti and Nepf, 2004]. Accordingly, a two-layer distribution of ε_s was assumed here (Figure 11a), where ε_s is lower within the roughness than above it.

The solution to equation (5) in the presence of large roughness was obtained by assuming the same uniform mean current, suspended sediment grain size, and the initializing condition as in the bare bed case. For this case, the SSC profile evolves from the uniform upstream concentration to a shape where the concentration increases with height above the bed (Figure 11b). This is qualitatively consistent with the SSC profiles observed in this experiment (Figure 9). Eventually (far downstream) the solution will converge to an exponential profile, analogous to that observed over a bare sandy bed but with a much lower concentration; for the fine suspended sediments (low settling velocity) observed in this study, that development would occur over large distances.

Thus, a likely explanation for the SSC profiles observed in the field experiment is that the narrow but aggressive surf zone located ~ 400 m upstream near the reef crest initially creates a well-mixed distribution of fine suspended sediment that slowly settles out of the water column. This sediment is advected by the cross-reef mean flows over and within the roughness. The reduced bed shear stress within the roughness leads to a reduction in c_0 , resulting in a net downward sediment flux by both diffusion and gravitational settling; the divergence in the vertical sediment flux is balanced by a convergence in the horizontal advective flux. It is this reduction in c_0 when compared to a larger upstream concentration that results in the reduced SSC values near the bed. These results suggest that the fine sediments ($D_{50} = 70$ μm) observed in suspension would likely include contributions from both local resuspension and sediment sourced upstream by advection. The fact that the coarse local bed sediment ($D_{50} = 240$ μm) is not in suspension is also consistent with this model, as the reduced bed shear stress within the roughness was found to be incapable of suspending this coarse sediment fraction.

5.2. Estimated Versus Measured Suspended Sediment Fluxes

Physical relationships that describe the hydrodynamics of bare sandy beds are still regularly applied to obtain quantitative estimates of sediment transport within ecosystems with large bottom roughness. It is therefore of particular interest to assess the sensitivity of predictions of SSFs (which integrate the effects of the modified concentration and velocity profiles), to these different definitions of the shear velocity. It is not our intention to conduct an exhaustive review of the applicability of key formulae, but instead to apply the different u_* values from this study in a one-dimensional (vertical) concentration profile model to simply assess the sensitivity of SSF predictions.

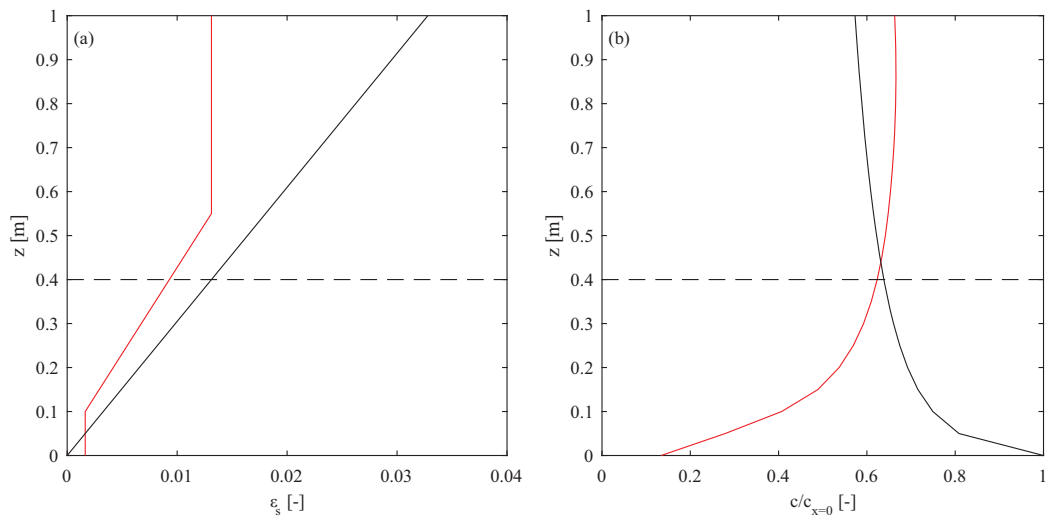


Figure 11. (a) Sediment mixing (diffusion) profile (ε_s) used in the advection-diffusion model. (b) Suspended sediment concentration (SSC) profiles from the advection-diffusion model with the concentration (c) normalized by the upstream boundary concentration ($c_{x=0}$). (black) No roughness layer in the model and (red) with a roughness layer in the model. The horizontal dotted line denotes the approximate height of the roughness in the model.

The depth-integrated Eulerian-mean SSFs were calculated from local estimates of SSF ($\bar{u}\bar{c}$) that were determined from time-averaged concentrations (\bar{c}) measured directly from the suction sample array and the colocated current velocity data (\bar{u}) measured at the time of sediment sampling by the ADP. We assume that the SSF at the lowest measurement point was representative of the fluxes further below, but recognize the flux could also be higher in this region. These discrete estimates were supplemented with SSFs calculated using 15 min bursts of velocity and the indirectly measured SSCs (calibrated back-scatter) from the ADP.

In order to predict the SSF for different u_* values, a SSC profile must be determined, which in turn requires prescription of the near-bed reference concentration (c_0). We specify the reference concentration using the same empirical model of Lee *et al.* [2004] used earlier (equation (6)). The form of the SSC profile is commonly represented by various solutions to equation (5) (e.g., exponential, power law, Rouse). We note that such SSC profiles only consider the diffusion and gravitational settling of sediment and do not take into account the advection of sediment from other areas. Here a commonly employed power law formulation was used:

$$c(z) = c_0 \left(\frac{z}{z_{ref}} \right)^{-P} \quad (7)$$

where z is the height above the bed and $P = w_s / \kappa u_{*,max}$ is the Rouse parameter. We note that this formulation results in a lower SSC higher in the water column than at the bed, which is not consistent with the observations in this experiment. However, we re-emphasize here that the purpose of the present analysis is to evaluate the extent to which the SSF estimates from established approaches (such as the one described by equation (7)) may deviate from the observations to assess the errors that can be introduced by applying conventional sediment transport formulations to these environments.

The horizontal velocity (\bar{u}) used to estimate the SSF was based on values measured by the ADP and we determined the SSFs following what was done earlier with the field data. We evaluated four cases, where the u_* that was used to calculate c_0 taken as either $u_{*,max,rough}$ or $u_{*,max,bed}$ and with the sediment grain size as either the D_{50} in suspension (70 μm) or the seabed D_{50} (240 μm). The shear velocity used to calculate the Rouse parameter was $u_{*,m,rough}$, which represents the greater mixing expected in the water column.

With the $D_{50} = 70 \mu\text{m}$ observed in suspension, the SSFs estimated using $u_{*,max,rough}$ are three orders of magnitude larger than those observed (Figure 12a), while for the seabed $D_{50} = 240 \mu\text{m}$ the estimated SSF is

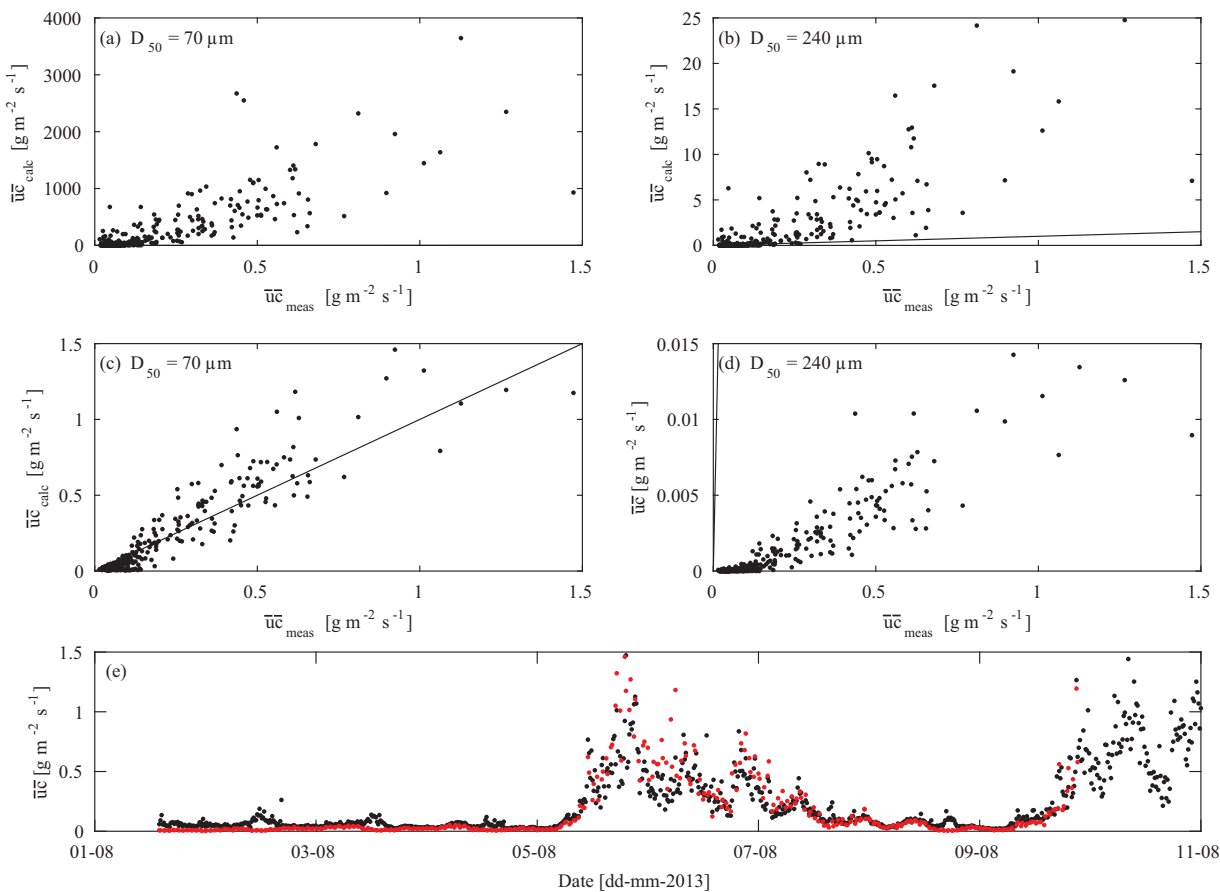


Figure 12. (a)–(d) Suspended sediment flux (SSF) on the reef flat compared with the SSF estimated using a power law profile with the reference concentration (c_0) formulation of Lee et al. [2004], $D_{50} = 70 \mu m$ or $240 \mu m$ and (top) $u_{*max,rough}$ and (middle) $u_{*max,bed}$. The solid black line indicates 1:1 agreement. (e) Estimated SSF (red) and measured SSF (black) for the duration of the experiment.

approximately 1–2 orders of magnitude too large (Figure 12b). In contrast, the SSF estimated using the reduced $u_{*max,bed}$ within the roughness and $D_{50} = 70 \mu m$ observed in suspension was of the correct order of magnitude (Figure 12c), an agreement that persisted throughout the experiment (Figure 12e). The SSF estimated with the reduced $u_{*max,bed}$ and the seabed $D_{50} = 240 \mu m$ was underestimated by 1–2 orders of magnitude (Figure 12d).

This sensitivity analysis demonstrates that established methods used to estimate SSF will substantially overestimate the flux when the shear stresses are estimated from hydrodynamic measurements that include the large form drag exerted by the roughness (i.e., when the impact of the roughness layer is not specifically considered). However, if the flow structure within the roughness is considered, the estimated SSF for this experiment was much closer and of the correct order of magnitude when the appropriate D_{50} in suspension is considered.

5.3. Implications for Sediment Transport Predictions

Existing studies of sediment dynamics in benthic ecosystems with large bottom roughness (e.g., coral reefs) still tend to focus on the long-standing framework for how sediment dynamics operate over bare sediment beds (e.g., occurs on sandy beaches). There have been considerable advances in predicting how hydrodynamic processes in coral reefs are modified by the presence of large bottom roughness (i.e., how the roughness affects circulation and wave transformation) with emphasis in these hydrodynamic studies generally on correctly representing the hydrodynamic properties above the roughness. This has typically been achieved by adjusting empirical friction parameters in models such as bottom drag coefficients to account for the large bottom roughness [e.g., Lowe et al., 2009a; Van Dongeren et al., 2013]. While this approach may yield a more “correct” reproduction of the hydrodynamic processes (at least above the canopy), this

approach will greatly overestimate the bed stresses that act on the sediment, which are directly responsible for driving sediment transport. Therefore, while the presence of the large roughness has the effect of increasing the predicted “bottom” stresses in hydrodynamic models, in reality the roughness would actually have the opposite effect on the sediment transport; that is, the roughness reduces bed shear stresses and thus suppresses sediment transport. While more research is required to develop robust predictive models of sediment transport in the presence of canopies, including how roughness modifies both the turbulent flow structure and bed shear stresses, as a starting point this study has demonstrated how reef roughness can result in a persistence of finer suspended sediments, lower SSCs and lower SSFs than would be predicted from using existing bare-bed sediment transport formulations.

6. Conclusions

The importance of sediment suspension and transport within coral reef ecosystems is well established; however, detailed measurements of sediment suspension and transport processes in these environments have been historically very limited. Consequently, the physics employed to describe these processes is typically based upon principles developed for sandy beach environments that are extended to reefs with large roughness (canopies) without a firm theoretical basis. We show that such models are likely to inaccurately quantify (at even an order of magnitude level) both suspended sediment concentrations and sediment fluxes.

In this study, we conducted a detailed field experiment to investigate the turbulent flow structure, SSCs, rates of suspended sediment transport, and size distributions of suspended sediment in a coral reef environment under combined wave-current flow conditions. The key results of this study are as follows:

1. A clear logarithmic velocity layer developed above the reef canopy but did not extend into the canopy; instead the velocity profile was inflected and hence the flow was reduced in the roughness (canopy) region adjacent to the bed.
2. The shear stresses that arise from the large canopy drag forces imposed on the overlying flow do not represent the actual shear stress imparted on the underlying bed sediment. The actual shear stress is substantially smaller than that on a bare bed, as demonstrated by the fineness of the suspended fraction and low SSC concentrations, which could not have been predicted by traditional models.
3. Simple estimation of the wave and current shear stress above and within large roughness vastly improves the predictive capability of established formulae for the grain size and concentration of suspended sediment in reef systems. However, further research is required to improve predictions of the concentration profiles observed in this experiment (higher concentrations above the roughness than within it) and to develop robust sediment transport formulations that can be applied to coral reefs and other analogous ecosystem with large bottom roughness.

Acknowledgments

AWP is grateful for the support of a Robert and Maude Gledden Postgraduate Research Award and by The Gowrie Trust Fund (2013, 2014). This project was funded by the Western Australia Marine Science Institute (WAMSI) Dredging Science Node (Theme 2/3), an Australian Research Council Future Fellowship (FT110100201), and ARC Discovery Project grant (DP140102026) to RJL, as well as the U.S. Geological Survey’s Coastal and Marine Geology Program. The authors thank Michael Cuttler, Sana Dandan, Jim Falter, Jeff Hansen, Malcolm McCulloch, Leonardo Ruiz Montoya, and Gundula Winter for their assistance during the experiment, and Johan Reynolds for his assistance in the implementation of the advection-diffusion model. We thank Shawn Harrison at the USGS who conducted an internal review of this manuscript, as well as the two anonymous reviewers who provided constructive feedback that helped us to improve the manuscript. Data sets analyzed in this manuscript are available from <http://doi.org/10.5281/zenodo.126670>.

References

- Ackerman, J. D., and A. Okubo (1993), Reduced mixing in a marine macrophyte canopy, *Funct. Ecol.*, 7(3), 305–309, doi:10.2307/2390209.
- Anthony, K. (2000), Enhanced particle-feeding capacity of corals on turbid reefs (Great Barrier Reef, Australia), *Coral Reefs*, 19(1), 59–67.
- Bagnold, R. (1966), An approach to the sediment transport problem from general physics, *US Geol. Surv. Prof. Pap.*, 422-I, 11–137, U.S. Gov. Print. Off., Washington, D. C.
- Baptist, M. J. (2005), *Modelling Floodplain Biogeomorphology*, TU Delft, Delft Univ. of Technol., Netherlands.
- Bosman, J. J., E. T. J. M. van der Velden, and C. H. Hulsbergen (1987), Sediment concentration measurement by transverse suction, *Coastal Eng.*, 11(4), 353–370, doi:10.1016/0378-3839(87)90033-0.
- Bouma, T., L. van Duren, S. Temmerman, T. Claverie, A. Blanco-Garcia, T. Ysebaert, and P. Herman (2007), Spatial flow and sedimentation patterns within patches of epibenthic structures: Combining field, flume and modelling experiments, *Cont. Shelf. Res.*, 27(8), 1020–1045.
- Canny, J. (1986), A computational approach to edge detection, *IEEE Trans. Pattern Anal. Mach. Intell.*, 8(6), 679–698, doi:10.1109/TPAMI.1986.4767851.
- Chen, Z., A. Ortiz, L. Zong, and H. Nepf (2012), The wake structure behind a porous obstruction and its implications for deposition near a finite patch of emergent vegetation, *Water Resour. Res.*, 48, W09517, doi:10.1029/2012WR012224.
- Cuttler, M., R. Lowe, J. Hansen, J. Falter, and A. W. M. Pomeroy (2015), Grainsize, composition and beform patterns in a fringing reef system, *Proc. Coastal Sediments*, editors by P. Wang, J. D. Rosati and J. Cheng, World Scientific, Singapore.
- Finnigan, J. (2000), Turbulence in plant canopies, *Annu. Rev. Fluid. Mech.*, 32(1), 519–571.
- Francis, J. (1973), Experiments on the motion of solitary grains along the bed of a water-stream, *Proc. R. Soc. London, Ser. A*, 332(1591), 443–471.
- Francois, R., and G. Garrison (1982), Sound absorption based on ocean measurements. Part II: Boric acid contribution and equation for total absorption, *J. Acoust. Soc. Am.*, 72(6), 1879–1890, doi:10.1121/1.388673.

- Gacia, E., T. C. Granata, and C. M. Duarte (1999), An approach to measurement of particle flux and sediment retention within seagrass (*Posidonia oceanica*) meadows, *Aquat. Bot.*, 65(1–4), 255–268, doi:10.1016/S0304-3770(99)00044-3.
- Ghisalberti, M. (2007), The impact of submerged canopies on open-channel hydrodynamics, in *Proceedings of the 5th International Symposium on Environmental Hydraulics*, edited by D. L. Boyer, Arizona State University, Tempe, Ariz.
- Ghisalberti, M., and H. Nepf (2004), The limited growth of vegetated shear layers, *Water Resour. Res.*, 40, W07502, doi:10.1029/2003WR002776.
- Goring, D., and V. Nikora (2002), Despiking acoustic doppler velocimeter data, *J. Hydraul. Eng.*, 128(1), 117–126, doi:10.1061/(ASCE)0733-9429(2002)128:1(117).
- Grant, W. D., and O. S. Madsen (1979), Combined wave and current interaction with a rough bottom, *J. Geophys. Res.*, 84(C4), 1797–1808.
- Ha, H., J.-Y. Maa, K. Park, and Y. Kim (2011), Estimation of high-resolution sediment concentration profiles in bottom boundary layer using pulse-coherent acoustic doppler current profilers, *Mar. Geol.*, 279(1–4), 199–209, doi:10.1016/j.margeo.2010.11.002.
- Hardy, T. A., and I. R. Young (1996), Field study of wave attenuation on an offshore coral reef, *J. Geophys. Res.*, 101(C6), 14,311–14,326, doi:10.1029/96JC00202.
- Hench, J. L., J. J. Leichter, and S. G. Monismith (2008), Episodic circulation and exchange in a wave-driven coral reef and lagoon system, *Limnol. Oceanogr. Methods*, 53(6), 2681–2694.
- Infantes, E., A. Orfila, G. Simarro, J. Terrados, M. Luhar, and H. Nepf (2012), Effect of a seagrass (*Posidonia oceanica*) meadow on wave propagation, *Mar. Ecol. Prog. Ser.*, 456, 63–72.
- James, C., A. Jordanova, and C. Nicolson (2002), Flume experiments and modelling of flow-sediment-vegetation interactions, in *International Association of Hydrological Sciences*, edited by F. J. Dyer, M. C. Thoms and J. M. Olley, IAHS Publ. No. 276, pp. 3–9, ISHS Press, Centre for Ecology and Hydrology, Wallingford, Oxfordshire, U. K.
- James, W. F., J. W. Barko, and M. G. Butler (2004), Shear stress and sediment resuspension in relation to submersed macrophyte biomass, *Hydrobiologia*, 515(1–3), 181–191.
- Jordanova, A., and C. James (2003), Experimental study of bed load transport through emergent vegetation, *J. Hydraul. Eng.*, 129(6), 474–478, doi:10.1061/(ASCE)0733-9429(2003)129:6(474).
- Kothiyari, U. C., H. Hashimoto, and K. Hayashi (2009), Effect of tall vegetation on sediment transport by channel flows, *J. Hydraul. Res.*, 47(6), 700–710.
- Le Bouteiller, C., and J. Venditti (2015), Sediment transport and shear stress partitioning in a vegetated flow, *Water Resour. Res.*, 51, 2901–2922, doi:10.1002/2014WR015825.
- Lee, G. h., W. B. Dade, C. T. Friedrichs, and C. E. Vincent (2004), Examination of reference concentration under waves and currents on the inner shelf, *J. Geophys. Res.*, 109, C02021, doi:10.1029/2002JC001707.
- Lowe, R. J., and J. L. Falter (2015), Oceanic forcing of coral reefs, *Annu. Rev. Mar. Sci.*, 7(18), 1–25, doi:10.1146/annurev-marine-010814-015834.
- Lowe, R. J., J. L. Falter, M. D. Bandet, G. Pawlak, M. J. Atkinson, S. G. Monismith, and J. R. Koseff (2005a), Spectral wave dissipation over a barrier reef, *J. Geophys. Res.*, 110, C04001, doi:10.1029/2004JC002711.
- Lowe, R. J., J. R. Koseff, and S. G. Monismith (2005b), Oscillatory flow through submerged canopies. 1: Velocity structure, *J. Geophys. Res.*, 110, C10016, doi:10.1029/2004JC002788.
- Lowe, R. J., U. Shavit, J. L. Falter, J. R. Koseff, and S. G. Monismith (2008), Modeling flow in coral communities with and without waves: A synthesis of porous media and canopy flow approaches, *Limnol. Oceanogr. Methods*, 53, 2668–2680, doi:10.4319/lom.2008.53.6.2668.
- Lowe, R. J., J. L. Falter, S. G. Monismith, and M. J. Atkinson (2009a), A numerical study of circulation in a coastal reef-lagoon system, *J. Geophys. Res.*, 114, C06022, doi:10.1029/2008JC005081.
- Lowe, R. J., J. L. Falter, S. G. Monismith, and M. J. Atkinson (2009b), Wave-driven circulation of a coastal reef-lagoon system, *J. Phys. Oceanogr.*, 39, 873–893.
- Luhar, M., S. Couto, E. Infantes, S. Fox, and H. Nepf (2010), Wave-induced velocities inside a model seagrass bed, *J. Geophys. Res.*, 115, C12005, doi:10.1029/2010JC006345.
- Neary, V. S., S. Constantinescu, S. Bennett, and P. Diplas (2011), Effects of vegetation on turbulence, sediment transport, and stream morphology, *J. Hydraul. Eng.*, 138(9), 765–776.
- Nepf, H., M. Ghisalberti, B. White, and E. Murphy (2007), Retention time and dispersion associated with submerged aquatic canopies, *Water Resour. Res.*, 43(4), W04422, doi:10.1029/2006WR005362.
- Nepf, H. M. (2012), Flow and transport in regions with aquatic vegetation, *Annu. Rev. Fluid. Mech.*, 44, 123–142.
- Ogston, A. S., C. D. Storlazzi, M. E. Field, and M. K. Presto (2004), Sediment resuspension and transport patterns on a fringing reef flat, Molokai, Hawaii, *Coral Reefs*, 23, 559–569, doi:10.1007/s00338-004-0415-9.
- Pomeroy, A. W. M. (2016), Tantabiddi sediment dynamics experiment (Ninglao Reef): Hydrodynamic and suspended sediment data [data set], Zenodo, doi:10.5281/zenodo.126670.
- Pomeroy, A. W. M., R. J. Lowe, G. Symonds, A. Van Dongeren, and C. Moore (2012), The dynamics of infragravity wave transformation over a fringing reef, *J. Geophys. Res.*, 117, C11022, doi:10.1029/2012JC008310.
- Presto, M. K., A. S. Ogston, C. D. Storlazzi, and M. E. Field (2006), Temporal and spatial variability in the flow and dispersal of suspended sediment on a fringing reef flat, Molokai, Hawaii, *Estuarine Coastal Shelf Sci.*, 67, 67–81, doi:10.1016/j.ecss.2005.10.015.
- Prosser, I. P., W. E. Dietrich, and J. Stevenson (1995), Flow resistance and sediment transport by concentrated overland flow in a grassland valley, *Geomorphology*, 13(1), 71–86.
- Raupach, M. R., R. A. Antonia, and S. Rajagopalan (1991), Rough-wall turbulent boundary layers, *Appl. Mech. Rev.*, 44(1), 1–25, doi:10.1115/1.3119492.
- Richards, S., A. Heathershaw, and P. Thorne (1996), The effect of suspended particulate matter on sound attenuation in seawater, *J. Acoust. Soc. Am.*, 100(3), 1447–1450.
- Rosman, J. H., and J. L. Hench (2011), A framework for understanding drag parameterizations for coral reefs, *J. Geophys. Res.*, 116, C08025, doi:10.1029/2010JC006892.
- Roth, M. S. (2014), The engine of the reef: Photobiology of the coral-algal symbiosis, *Front. Microbiol.*, 5, 422, doi:10.3389/fmicb.2014.00422.
- Shaw, W. J., and J. H. Trowbridge (2001), The direct estimation of near-bottom turbulent fluxes in the presence of energetic wave motions, *J. Atmos. Oceanic Technol.*, 18(9), 1540–1557.
- Shields, A. (1936), *Application of Similarity Principles and Turbulence Research to Bed-Load Movement*, California Inst. of Technol., Pasadena, Calif.
- Smith, J. D., and S. McLean (1977), Boundary layer adjustments to bottom topography and suspended sediment, *Elsevier Oceanogr. Ser.*, 19, 123–151.

- Soulsby, R. (1997), *Dynamics of Marine Sands: A Manual for Practical Applications*, Thomas Telford, London.
- Soulsby, R., and S. Clarke (2005), Bed shear-stresses under combined waves and currents on smooth and rough beds, *Rep. TR137*, HR Wallingford Ltd., Wallingford, U. K.
- Storlazzi, C. D., A. S. Ogston, M. H. Bothner, M. E. Field, and M. K. Presto (2004), Wave- and tidally-driven flow and sediment flux across a fringing coral reef: Southern Molokai, Hawaii, *Cont. Shelf. Res.*, 24(12), 1397–1419, doi:10.1016/j.csr.2004.02.010.
- Storlazzi, C. D., M. E. Field, M. H. Bothner, M. K. Presto, and A. E. Draut (2009), Sedimentation processes in a coral reef embayment: Hanalei Bay, Kauai, *Mar. Geol.*, 264, 140–151, doi:10.1016/j.margeo.2009.05.002.
- Suhayda, J. N., and H. H. Roberts (1977), Wave action and sediment transport on fringing reefs, in *Proceedings of Thirrd International Coral Reef Symposium*, edited by D. L. Taylor, Rosenstiel Sch. of Mar. and Atmos. Sci., Miami, Fla.
- Symonds, G., K. P. Black, and I. R. Young (1995), Wave-driven flow over shallow reefs, *J. Geophys. Res.*, 100(C2), 2639–2648, doi:10.1029/94JC02736.
- Van Dongeren, A., R. Lowe, A. Pomeroy, D. M. Trang, D. Roelvink, G. Symonds, and R. Ranasinghe (2013), Numerical modeling of low-frequency wave dynamics over a fringing coral reef, *Coastal Eng.*, 73, 178–190, doi:10.1016/j.coastaleng.2012.11.004.
- van Katwijk, M. M., A. R. Bos, D. C. R. Hermus, and W. Suykerbuyk (2010), Sediment modification by seagrass beds: Muddification and sandification induced by plant cover and environmental conditions, *Estuarine Coastal Shelf Sci.*, 89(2), 175–181, doi:10.1016/j.ecss.2010.06.008.
- Van Rijn, L. C. (1984), Sediment transport, Part II: Suspended load transport, *J. Hydraul. Eng.*, 110(11), 1613–1641.
- Van Rijn, L. C. (1993), *Principles of Sediment Transport in Rivers, Estuaries and Coastal Seas*, Aqua Publ., Amsterdam.
- Van Rijn, L. C. (2007), Unified view of sediment transport by currents and waves. I: Initiation of motion, bed roughness, and bed-load transport, *J. Hydraul. Eng.*, 133(6), 649–667.
- Ward, L. G., W. M. Kemp, and W. R. Boynton (1984), The influence of waves and seagrass communities on suspended particulates in an estuarine embayment, *Mar. Geol.*, 59(1), 85–103.
- Weber, M., D. de Beer, C. Lott, L. Polerecky, K. Kohls, R. M. Abed, T. G. Ferdelman, and K. E. Fabricius (2012), Mechanisms of damage to corals exposed to sedimentation, *Proc. Natl. Acad. Sci. U. S. A.*, 109(24), E1558–E1567.
- Wiberg, P. L. (1995), A theoretical investigation of boundary layer flow and bottom shear stress for smooth, transitional, and rough flow under waves, *J. Geophys. Res.*, 100(C11), 22,667–22,679.
- Widdows, J., N. D. Pope, M. D. Brinsley, H. Asmus, and R. M. Asmus (2008), Effects of seagrass beds (*Zostera noltii* and *Z. marina*) on near-bed hydrodynamics and sediment resuspension, *Mar. Ecol. Prog. Ser.*, 358, 125–136.
- Zeller, R. B., F. J. Zarama, J. S. Weitzman, and J. R. Koseff (2015), A simple and practical model for combined wave-current canopy flows, *J. Fluid Mech.*, 767, 842–880.